JGR Space Physics

RESEARCH ARTICLE
10.1029/2025JA034907

Compression of Mercury's Dayside Magnetopause to the Surface: A Three-Dimensional Model of Magnetospheric Structure and Dynamics

Georg Glebe[1], **C. Michael Haynes**[1], **and Sven Simon**[1,2]

[1]School of Earth and Atmospheric Sciences, Georgia Institute of Technology, Atlanta, GA, USA, [2]School of Physics, Georgia Institute of Technology, Atlanta, GA, USA

Key Points:

- We model Mercury's space environment when exposed to a Coronal Mass Ejection that triggers a Disappearing Dayside Magnetosphere (DDM) event
- Under DDM conditions, a bow shock forms above Mercury's low-latitude dayside for a northward but not for a southward upstream magnetic field
- Comparing model results and MErcury Surface Space ENvironment, GEochemistry, and Ranging data reveals that magnetotail twisting may cause a displacement of the neutral sheet during DDM events

Correspondence to:
G. Glebe,
gglebe3@gatech.edu

Citation:
Glebe, G., Haynes, C. M., & Simon, S. (2026). Compression of Mercury's dayside magnetopause to the surface: A three-dimensional model of magnetospheric structure and dynamics. *Journal of Geophysical Research: Space Physics*, *131*, e2025JA034907. https://doi.org/10.1029/2025JA034907

Received 25 NOV 2025
Accepted 2 FEB 2026

Abstract We apply a hybrid model (kinetic ions, fluid electrons) to provide context for MErcury Surface Space ENvironment, GEochemistry, and Ranging (MESSENGER) observations of Disappearing Dayside Magnetosphere (DDM) events at Mercury. Such events have been observed on four occasions and are caused by Coronal Mass Ejections completely removing the dayside magnetopause (MP) through erosion and compression. We investigate how different Interplanetary Magnetic Field (IMF) orientations, resulting in different reconnection rates, influence Mercury's magnetosphere under these extreme conditions. The model uses constant upstream conditions and the highest ram pressure reported for any DDM event to date. Our results are: (a) Under DDM conditions, a bow shock forms above Mercury's low-latitude surface for northward or duskward IMF orientation. (b) However, when the IMF points southward, the solar wind impacts unhindered onto the equatorial dayside surface, and a shock develops only at high latitudes. In this case, the IMF is antiparallel to the dayside planetary field, and any closed field lines in the upstream hemisphere are eroded through reconnection. Hence, despite the favorable IMF orientation, no return plasma flow forms: protons largely travel along the outer flanks of the MP toward downstream. (c) The wakeside draping pattern seen during a DDM event in 2013 is consistent with a drop in upstream pressure by at least 30% while MESSENGER passed through the magnetotail. The observed neutral sheet position suggests that the IMF changed from duskward to dawnward orientation during the spacecraft's passage through the magnetosphere. (d) Magnetotail twisting may have caused the southward displacement of the neutral sheet observed during the 2013 event.

1. Introduction

Mercury is the smallest and innermost planet of the solar system, with an orbital period of 88 days. A weak intrinsic magnetic field was first reported from observations of the Mariner 10 spacecraft (Ness et al., 1974) and investigated in more detail with the MErcury Surface, Space ENvironment, GEochemistry, and Ranging (MESSENGER) magnetometer (Anderson et al., 2007). It was found that the planet's internal field can be represented by a southward dipole moment with magnitude 195 nT $\cdot R_M^3$, where $R_M = 2440$ km is Mercury's radius. The dipole axis is anti-aligned with the spin axis, deviating by less than 1°, and the dipole is offset by approximately 0.2 R_M northward from the planet's center (Anderson et al., 2012). Alternatively, this field can be represented by a superposition of *centered* dipole and quadrupole moments (e.g., Anderson et al., 2011; Anderson et al., 2012; Thébault et al., 2018; Töpfer et al., 2022; Wardinski et al., 2019).

The MESSENGER spacecraft was in orbit around Mercury from March 2011 until April 2015. Its (8 − 12) h long polar orbit was highly elliptical with the periapsis in the northern hemisphere and closest approach altitudes between 200 km and 500 km. The asymmetry in the spacecraft's trajectory resulted in a better coverage of Mercury's immediate space environment in the northern hemisphere. MESSENGER collected detailed plasma and magnetic field data within the Hermean magnetosphere, which is qualitatively similar to Earth's. However, Mercury's surface magnetic field is about a factor of 150 weaker than Earth's (Anderson et al., 2011; Finlay et al., 2010) and the solar wind ram pressure at Mercury $p_{SW} = \rho u^2$ (where ρ: mass density, u: bulk velocity) is an order of magnitude stronger (Korth et al., 2018; Sun et al., 2022). Therefore, the size of the magnetosphere, compared to the planet's radius, is much smaller at Mercury than at Earth. The magnetopause (MP) and bow shock (BS) possess average subsolar standoff distances from the dipole center of 1.45 R_M and 1.96 R_M, respectively (Winslow et al., 2013).

Extreme solar wind events, such as interplanetary Coronal Mass Ejections (ICMEs), can compress the Hermean magnetosphere. Winslow et al. (2015) identified 61 such events in MESSENGER magnetometer data collected between 2011 and 2014. Subsequently, Winslow et al. (2017) extended this database by including eight additional events from 2015, now covering the entire orbital phase of MESSENGER. By identifying MP crossings in magnetometer data for all events and fitting the Shue et al. (1997) MP model to the data set, they determined the average subsolar standoff distance across all 69 events to be 1.25 R_M. This value is about 14% smaller than under nominal solar wind conditions (Winslow et al., 2013). By fitting the MP model to individual events, Winslow et al. (2017) also showed that the MP should have intersected Mercury's surface during 29% of the ICME impacts. However, they did not provide in situ evidence of such a strong compression.

Slavin et al. (2014) studied three MESSENGER observations from events where Mercury's MP was compressed, but still remained above the surface at all latitudes; these were referred to as Highly Compressed Magnetosphere (HCM) events. Two of these events were caused by ICMEs and one by a high-speed solar wind stream. By assuming balance between the solar wind ram pressure and the planetary magnetic pressure at the MP, Slavin et al. (2014) determined upstream pressures of 51, 53, and 65 nPa for the three HCM events, compared to the nominal value of 14.3 nPa (Winslow et al., 2013).

During a Disappearing Dayside Magnetosphere (DDM) event, Mercury's magnetosphere is compressed even stronger and the dayside MP would reside below the planet's surface. Slavin et al. (2019) used data from the MESSENGER magnetometer and the Fast Imaging Plasma Spectrometer (FIPS, Andrews et al., 2007), and found four such events throughout the entire orbital phase of the mission, sampled in 2011 (DOY 288), 2013 (DOY 334 − 335), 2014 (DOY 44), and 2015 (DOY 83 − 84). To identify these events, the authors searched observations from the dayside segment of each orbit according to two criteria: (a) no northward magnetic field component is measured, as such a component would correspond to the planetary dipole field, and (b) FIPS data only shows proton energy spectra that are consistent with those of the nominal shocked magnetosheath. While criterion (a) implies that MESSENGER did not encounter any closed planetary field lines on the low-latitude dayside, such field lines could still exist below the spacecraft's orbit at altitudes lower than 250 − 300 km.

During all four observed DDM events, the MP crossings occurred at high latitudes of 66° to 80° and the subsolar standoff distance was found to be below Mercury's surface. The BS was compressed to about 1.5 R_M from the dipole center, corresponding to 75% of the value under nominal solar wind conditions (Winslow et al., 2013). Hence, for all studied cases the BS remained above the surface. The Interplanetary Magnetic Field (IMF) reached magnitudes of (70 – 150) nT for the four DDM events examined by Slavin et al. (2019), compared to a nominal IMF strength smaller than 40 nT at Mercury (James et al., 2017; Slavin & Holzer, 1981). During all DDM events, the IMF was tilted against the planet's dipole axis, but possessed a larger north-south component than under nominal conditions (Slavin & Holzer, 1981). When traveling through the dayside magnetosheath, MESSENGER always observed a dominant southward field component up to twice as strong as the components perpendicular to the north-south axis. Since the planetary dipole field in the subsolar region points northward, the strong southward IMF facilitates the occurrence of reconnection in that region while a northward IMF would inhibit it. Therefore, Slavin et al. (2019) proposed that MP erosion due to dayside reconnection may contribute to the absence of the low-latitude MP at the dayside. By assuming pressure balance across the MP, the solar wind ram pressure during the four DDM events was found to range from 142 nPa to 289 nPa. These values are at least three times as high as for the HCM events studied by Slavin et al. (2014) and about an order of magnitude larger than for nominal solar wind conditions (Winslow et al., 2013).

Mercury's plasma environment during the 2013 DDM event was sampled along two consecutive MESSENGER orbits. While the analysis of Slavin et al. (2019) considered data from the second orbit, Winslow et al. (2020) focused on observations from the first orbit and estimated a solar wind ram pressure of (385 ± 177) nPa. This range represents the highest ram pressures reported for any DDM event at Mercury so far. The range of pressures obtained by Winslow et al. (2020) for the first orbit is a factor of 1.1–3.1 larger than the 182 nPa derived by Slavin et al. (2019) for the second orbit, implying that the solar wind conditions during Mercury's exposure to the ICME may not have been stationary. No region of northward planetary field lines was sampled during the dayside segment of the orbit studied by Winslow et al. (2020) and the MP was crossed at a near-polar latitude of 84°. These observations were interpreted as a collapsed dayside MP with approximately 50% of the planetary surface directly exposed to the solar wind. Magnetometer data suggests that for this orbit Mercury's low-latitude BS was compressed below the surface as well.

We emphasize that the range of pressure values derived by Slavin et al. (2019) and Winslow et al. (2020) is afflicted with significant uncertainties: these estimations rely on the pressure balance method from Spreiter et al. (1966); that is, the pressure is inferred indirectly from magnetic field measurements. The values provided by these authors are not based on, for example, in situ observations with a particle detector. A pressure of 385 nPa, as proposed by Winslow et al. (2020), is at the extreme upper end of all values published for Mercury to date.

By applying a magnetohydrodynamic (MHD) model, Kabin et al. (2000) found the dayside MP to intersect the planet's surface for a ram pressure of 148 nPa, consistent with MESSENGER magnetometer observations from the DDM event in 2011 (Slavin et al., 2019). Exner et al. (2018) used the AIKEF hybrid model (Adaptive Ion Kinetic Electron Fluid; see Müller et al., 2011) to analyze the magnetometer time series from one of the HCM events identified by Slavin et al. (2014). Different upstream conditions were required to reproduce the features seen in the magnetic field from the dayside and nightside segments of that orbit. The authors concluded that the solar wind conditions inside the ICME were highly variable over time scales of only a few minutes.

Using the Amitis hybrid model, Fatemi et al. (2020) found the dayside MP to be compressed to the planet's surface for northward IMF with a solar wind ram pressures of 72 nPa, which is only half of the lowest value derived from MESSENGER observations (Slavin et al., 2019). The disparity may partially stem from their model treating Mercury as an uniform, resistive obstacle to the solar wind. However, Mercury possesses a highly conductive iron core of radius 0.8 R_M (e.g., Hauck et al., 2013). Time-varying currents in the planet's space environment generate an inductive response in the core that may enhance Mercury's internal magnetic field. In this way, induction can contribute to the counter pressure that keeps the MP away from the surface (e.g., Dong et al., 2019; Glassmeier et al., 2007; Grosser et al., 2004; Heyner et al., 2016; Zomerdijk-Russell et al., 2021).

Jia et al. (2019) applied a time-dependent MHD model to study the influence of reconnection on the MP position during HCM events. To trigger induction in Mercury's core, their model runs were initiated with a ram pressure of 3 nPa and, after a stationary state had been reached, the pressure was increased to four different values in the range from 8 nPa to 107 nPa. After this enhancement in pressure, the model runs were continued until a new stationary state was achieved. For each pressure value, runs were carried out for several different IMF setups: northward, southward, and no IMF at all. For the southward case, the authors also considered a model setup with a uniformly high resistivity within Mercury's interior, thereby suppressing induction effects. In all setups, the distance of the MP to the planet decreased in the following order: no IMF, northward IMF, southward IMF with induction, southward IMF without induction (Jia et al., 2019). For a southward IMF and a pressure of 107 nPa, corresponding to 75% of the lowest value reported by Slavin et al. (2019), the entire dayside MP was compressed to Mercury's surface. Conversely the MP still remained above the surface for a northward IMF. Jia et al. (2019) also showed that, without the core's inductive response, the dayside MP already collapses at a ram pressure of 56 nPa. In this way, the authors demonstrated that both induction and reconnection are important competing processes in shaping Mercury's dayside magnetosphere: while reconnection erodes the MP, induction counteracts the MP compression.

By applying a hybrid model, Guo et al. (2023) studied Mercury's magnetosphere during DDM events. They performed seven model runs, covering solar wind ram pressures from 8 nPa up to 107 nPa. All runs were carried out with a southward or northward IMF of magnitude 34 nT or 50 nT. For a southward IMF with 34 nT magnitude and a ram pressure of 25 nPa, the authors found the dayside MP to reside below Mercury's surface. This value is much lower than the pressures reported by other models (Fatemi et al., 2020; Jia et al., 2019) and observations (Slavin et al., 2019; Winslow et al., 2020). For the same upstream pressure and magnetic field magnitude, but a northward IMF, the dayside MP in the model of Guo et al. (2023) did not disappear.

In this study, we apply the AIKEF hybrid model (Müller et al., 2011) to gain a deeper understanding of the three-dimensional magnetospheric structure and the influence of solar wind parameters during DDM events. Even under nominal solar wind conditions Mercury's magnetosphere possesses a north-south asymmetry with respect to the planet's geographic equatorial plane. Such asymmetries can be caused by, for example, the northward dipole offset, generating a higher surface field strength in the northern hemisphere than in the southern (Winslow et al., 2014). In consequence, the MP is closer to the planet's surface south of the equator (Zhong et al., 2015). To gain straightforward access to the involved physics, we therefore consider several idealized model setups with the IMF being parallel, anti-parallel, or perpendicular to Mercury's dipole axis. In addition, to isolate the influence of the northward dipole offset, we also compare setups with the magnetic moment placed at the planet's center and setups taking the offset into account. Unlike Guo et al. (2023), we consider pressures within the range estimated

for the observed DDM events (Slavin et al., 2019; Winslow et al., 2020). We also conduct an extensive parameter study, comparing model output against magnetometer observations from the 2013 DDM event. Comparisons between model output and MESSENGER data from any DDM event have not yet been presented in the literature. Finally, we investigate the dynamics of plasma transport through Mercury's magnetosphere under DDM conditions.

This work is organized as follows: in Section 2, we introduce the AIKEF hybrid model and discuss the numerical and physical parameters used for this study. In Section 3, we present results from controlled model runs with idealized solar wind conditions, as well as a comparison of modeled time series to MESSENGER observations during the 2013 DDM event. Finally, we summarize our major results in Section 4.

2. Hybrid Plasma Model AIKEF

We apply the three-dimensional AIKEF hybrid model (Müller et al., 2011) to calculate the structure of Mercury's space environment during DDM events. AIKEF has been utilized in numerous preceding studies to model Mercury's interaction with the solar wind (Aizawa et al., 2021; Exner et al., 2018, 2020, 2024; Müller et al., 2011, 2012; Teubenbacher, Exner et al., 2025; Teubenbacher, Narita et al., 2025; Teubenbacher et al., 2024; Töpfer, Narita, Glassmeier et al., 2021; Töpfer, Narita, Exner et al., 2021; Töpfer et al., 2020; Werner et al., 2022), as well as the plasma interaction with other magnetized objects like asteroids (Simon et al., 2006) and Ganymede (Haynes et al., 2025; Stahl et al., 2023).

We use the Mercury-Solar-Orbital (MSO) coordinate system: the origin of this Cartesian system coincides with the center of Mercury, the X axis points toward the Sun and the Z axis is oriented northward. The Y axis completes the right-handed coordinate system and is anti-parallel to the planet's orbital motion around the Sun. The unit vectors of this system read $\boldsymbol{e}_X$, $\boldsymbol{e}_Y$, and $\boldsymbol{e}_Z$. For all setups considered, the model domain has extensions of $-4\ R_M \leq X \leq 4\ R_M$ and $-5\ R_M \leq Y, Z \leq 5\ R_M$. This box is discretized with a hierarchical Cartesian mesh that has a highest resolution of $\Delta X = 0.019\ R_M$ and $\Delta Y = \Delta Z = 0.020\ R_M$ within the cuboid $-3\ R_M \leq X \leq 2\ R_M$ and $-3\ R_M \leq Y, Z \leq 3\ R_M$. Outside of this region the cell size is twice as large. The volume of the maximum grid resolution encompasses the entire dayside interaction region, and the cells within this cuboid are smaller than solar wind proton gyroradii for all runs. In each cell, the solar wind protons are represented by about 25 macroparticles. The timestep in the model is set to $0.002\ T_g$, where $T_g = 0.6$ s is the gyroperiod of protons in the solar wind.

Models of Mercury's interior, obtained from gravity field observations, suggest that the planet consists of two distinct parts: a highly conducting iron core of radius $0.8\ R_M$ and a resistive mantle on top of it (e.g., Hauck et al., 2013; Siegfried & Solomon, 1974; Smith et al., 2012). In the AIKEF model, theses regions are represented by a radially symmetric resistivity profile, analogous to previous studies by, e.g., Müller et al. (2012), Jia et al. (2015) and Dong et al. (2019). Consistent with the approach of Jia et al. (2015), the mantle resistivity is set to $1.25 \cdot 10^7\ \Omega$m in the region $0.8\ R_M \leq r \leq 1.0\ R_M$, with $r = \sqrt{X^2 + Y^2 + Z^2}$ denoting the radial distance from the origin of the MSO system. In our model, Mercury's core is located inside of $r = 0.8\ R_M$ and the resistivity linearly drops to zero within two grid cells of this boundary. Analogous to Jia et al. (2015; Section 2.2) and Guo et al. (2023; Section 2), the magnetic field inside the core is not advanced in time. This approach provides an accurate representation of magnetic field diffusion through Mercury's interior: assuming a conductivity of $\sigma = 10^5$ S m^{-1} for the core (e.g., Heyner et al., 2010, 2011; Suess & Goldstein, 1979), the IMF would need $\mu_0 \sigma (2 \cdot 0.8\ R_M)^2 \approx 10^4$ years to diffuse through the core. This value exceeds the travel time of the solar wind through Mercury's interaction region (and the duration of our model runs) by 10 orders of magnitude. Any protons that hit the planet's surface at $r = 1\ R_M$ are removed from the simulation.

Detailed information on the model setups can be found in Table 1. Runs #1 − #5 use the average solar wind ram pressure from the first orbit of the 2013 DDM event, which is the highest reported value at Mercury to date (Winslow et al., 2020). We first consider several idealized setups that align the IMF with a coordinate axis of the MSO system (runs #1 − #4). In addition, runs #1 − #3 include a centered planetary magnetic moment to isolate the influence of the offset dipole. These initial configurations provide context for the analysis of run #5, which uses an inclined IMF vector observed by MESSENGER during the 2013 event. In addition, we have performed a parameter study with IMF vectors and ram pressures within the uncertainty range for this event. Since the IMF is derived directly from the observations, we are going to introduce these additional runs later in Section 3.3. To

Table 1
Solar Wind Conditions and Model Setup for the AIKEF Runs

Parameter	Symbol [unit]	Run #1	Run #2	Run #3	Run #4	Run #5	Run #6
Bulk velocity	u_{SW} [km s^{-1}]	800	800	800	800	800	900
Proton/electron density	n_{SW} [cm^{-3}]	360	360	360	360	360	105
Ram pressure[a]	p_{SW} [nPa]	385	385	385	385	385	142
Proton/electron temperature	T_{SW} [10^{5}K]	2	2	2	2	2	2
IMF vector	$\boldsymbol{B}_{SW}$ [nT]	(0, 0, 115)	(0, 115, 0)	(0, 0, −115)	(0, 0, −115)	(−108, −29, −25)	(0, 0, −68)
IMF magnitude	$\lvert\boldsymbol{B}_{SW}\rvert$ [nT]	115	115	115	115	115	68
Proton gyroradius	r_g [R_M]	0.03	0.03	0.03	0.03	0.03	0.06
Alfvén velocity	v_A [km s^{-1}]	132	132	132	132	132	145
Sonic velocity	v_S [km s^{-1}]	81	81	81	81	81	81
Magnetosonic velocity	v_{MS} [km s^{-1}]	155	155	155	155	155	166
Alfvénic Mach number	M_A	6.05	6.05	6.05	6.05	6.05	6.22
Sonic Mach number	M_S	9.84	9.84	9.84	9.84	9.84	11.08
Magnetosonic Mach number	M_{MS}	5.16	5.16	5.16	5.16	5.16	5.42
Proton/electron plasma beta	β_{SW}	0.19	0.19	0.19	0.19	0.19	0.16
Dipole offset in the (+Z) direction	[R_M]	0	0	0	0.2	0.2	0

[a]The ram pressure is related to the proton density and bulk velocity via $p_{SW} = n_{SW}\, m_p\, u_{SW}^2$.

study the influence of the solar wind ram pressure on the magnetospheric structure, run #6 applies the lowest ram pressure derived for any DDM event so far (Slavin et al., 2019). All setups use constant upstream solar wind conditions. Therefore, they do not contain an inductive response of Mercury's core as studied by, for example, Jia et al. (2019). However, the model does include induction driven by time-dependent processes *within* Mercury's magnetosphere, such as reconnection or Kelvin-Helmholtz waves.

For runs #1 − #5 we apply the solar wind bulk velocity estimated by Winslow et al. (2015) for the corresponding ICME, namely $u_{SW} = 800$ km s^{-1}. This value is the average transit speed of the ICME between its launch at the Sun, observed by STEREO, and subsequent arrival at Mercury, seen by MESSENGER. We still caution the reader regarding the uncertainties of this approach. STEREO data do not capture the actual, three-dimensional structure of the ICME nor its time evolution as it travels from the Sun toward Mercury. Due to the position of FIPS behind MESSENGER's sunshade, calculation of plasma moments, such as the density or temperature, is often infeasible in the solar wind upstream of Mercury (Raines et al., 2011). Therefore, we use the ram pressure of about $p_{SW} = 385$ nPa, estimated from assuming balance with the magnetic pressure at the MP (Winslow et al., 2020). Combined with the value of the bulk velocity, this pressure yields a solar wind proton density of $n_{SW} = 360$ cm^{-3} (Winslow et al., 2020). We determined the IMF vector for this event by averaging magnetometer observations over the interval from 16:35 UTC until 16:40 UTC on 30 November 2013 (see Figure 1 of Winslow et al., 2020). In this segment of the orbit, MESSENGER was located upstream of the BS. The resulting vector $\boldsymbol{B}_{SW} = (-108, -29, -25)$ nT has a magnitude of 115 nT and possesses a tilt angle of about 20° against the X axis. We use the measured IMF magnitude for the runs #1 − #5, but an idealized orientation in the first four runs, namely a magnetic field pointing northward, duskward, or southward. In this way, we can systematically assess how different dayside reconnection rates contribute to the results. While in run #1 the IMF is oriented northward and therefore inhibits reconnection, the anti-parallel orientation in run #3 facilitates it (Sun, Slavin, Smith, et al., 2020; Zomerdijk-Russell et al., 2023). Near the dawn and dusk flanks of the magnetosphere, the planetary dipole field possesses a non-zero B_Y component. Therefore, a duskward oriented IMF (run #2) can cause localized reconnection in these regions.

While we apply a centered planetary magnetic moment of magnitude 195 nT $\cdot R_M^3$ in the first three runs, we use the reported northward offset dipole for Mercury in run #4. For this setup we again implement an IMF pointing in the (−Z) direction. In this way, we can directly compare the results of runs #3 and #4 to study how the dipole

displacement contributes to the physical picture of DDM events. For run #5 we apply the offset dipole and a magnetic field configuration measured by MESSENGER to provide context for the interpretation of the observed magnetometer data during the 2013 DDM event. This setup is our baseline for the model-data comparison. Additional runs will be introduced in Section 3.3.

Run #6 aims to assess how Mercury's magnetosphere during DDM events is affected by the ram pressure. Therefore, we use solar wind parameters from the 2011 DDM event with the lowest solar wind pressure estimated for such a scenario to date (Slavin et al., 2019). We combine this value with the bulk velocity reported by Winslow et al. (2015) to calculate the upstream density given in Table 1. To facilitate direct comparison to run #3, we again consider a centered internal dipole at Mercury and the IMF pointing in the $(-Z)$ direction. The magnetic field magnitude is obtained by averaging over the interval from 14:15 UTC until 14:20 UTC on 15 October 2011 where MESSENGER was located upstream of Mercury's BS (see Figure 4 of Slavin et al., 2019).

No in situ measurements of the solar wind temperature upstream of Mercury are available during the DDM events (see Raines et al., 2011). However, the MHD modeling study of Varela et al. (2016) showed that for upstream temperatures between $2 \cdot 10^4$K and $2 \cdot 10^5$K the MP position remained largely unchanged. For this reason, our study applies the temperature under nominal solar wind conditions ($2 \cdot 10^5$K, e.g., Slavin & Holzer, 1981; Sun et al., 2022). This value was also used in previous studies of HCM and DDM events (e.g., Exner et al., 2018; Guo et al., 2023; Jia et al., 2019). The solar wind is clearly supermagnetosonic for all setups, with Alfvénic and magnetosonic Mach numbers (see Table 1) slightly larger than the values determined for nominal conditions: $M_A \in [3.9, 5.7]$, and $M_{MS} \in [3.18, 4.16]$, respectively (Sarantos & Slavin, 2009; Slavin & Holzer, 1981). The total plasma beta, defined as the sum of the values for electrons and protons, is between 0.32 and 0.38 for all runs, that is, less than unity. These values are also below the range of [0.5,0.9] reported for non-ICME conditions (Slavin & Holzer, 1981).

The number density ratio of helium ions to protons in the solar wind, under nominal conditions, is around 5% (e.g., Hundhausen, 1970). Using STEREO-A observations near 1 AU, Winslow et al. (2020) reported a helium-to-proton ratio of up to 33% for the ICME that caused the 2013 DDM event. However, in our study we assume the solar wind to consist entirely of protons and electrons. Since in situ measurements of the upstream plasma density could not be conducted during the DDM events (Raines et al., 2011; Slavin et al., 2019; Winslow et al., 2020), the solar wind density is calculated from the published ram pressure and velocity. Decomposing the resulting average ion number density into contributions from protons and helium would not have a noticeable impact on our results: the mass-to-charge ratios of both ion species are very similar. In addition, the gyroradii of these species in the solar wind are smaller than Mercury's radius by more than an order of magnitude.

Mercury possesses a thin exosphere, composed of several neutral species. The mass density of sodium exceeds those of the other species by at least an order of magnitude (see McClintock et al., 2018, and references therein). Using FIPS data, Gershman et al. (2014) showed that ionized sodium, originating from the planet's exosphere, may contribute around 15% to the thermal pressure in Mercury's pre-midnight plasma sheet. To study the influence of Na^+ ions on the planet's magnetospheric structure, Exner et al. (2020) included the exosphere model of Gamborino et al. (2019) in AIKEF and then calculated the Na^+ production by scaling photoionization rates at Earth to Mercury's average orbital position. Exner et al. (2020) found that, to generate any discernible effect on the standoff distance of the MP, the neutral sodium density must exceed the values from Gamborino et al. (2019) by at least a factor of five, thereby producing Na^+ ion densities comparable to the highest values observed during DDM events. For this setup the MP was found to be displaced sunward by $0.1 - 0.3\ R_M$, compared to a model run with no sodium. However, Exner et al. (2020) studied the contribution of the sodium ions only for a low solar wind pressure of 2 nPa, which is two orders of magnitude smaller than the pressure range reported for DDM events (Slavin et al., 2019; Winslow et al., 2020). Therefore, the ratio of the counter pressure generated by sodium ions to the solar wind pressure is larger in their scenario than for an enhanced upstream ram pressure. Hence, the MP displacement reported by Exner et al. (2020) would likely be smaller for DDM events, and we refrain from including the exosphere in our model setup. If future observations, for example, by BepiColombo, reveal a significant contribution of Mercury's exosphere to the magnetospheric structure under DDM conditions, our results can be used to establish a "baseline" for the interpretation of such data sets.

3. Model Results for Mercury's Magnetosphere

3.1. Quasi-Stationary State for Centered Dipole

Figures 1 and 2 depict our model results for Mercury's magnetic and plasma environment. From left to right, the columns display the output from runs #1 − #3, which all include a centered planetary dipole. The first two rows of Figure 1 show the absolute value of the magnetic field $|\boldsymbol{B}|$ in the $X-Z$- and $X-Y$-planes. The third row depicts the B_X component and the fourth row the B_Z component in the planes through the center of the planet that contain the IMF vector and $\boldsymbol{e}_X$. Figure 2 shows two-dimensional cuts through the proton number density n. The first row shows the $X-Z$-plane, whereas the second row depicts the $X-Y$-plane. The model results are shown after 45 s of real time, corresponding to two passages of the unperturbed solar wind through the simulation domain. By this time, the modeled magnetosphere has achieved a quasi-stationary state.

The arrows in Figure 2 mark the positions of the modeled MP (cyan) and BS (bold red), which we identified downstream of Mercury from localized jumps in the number density. The parabolic BS is denoted by an increased proton number density on Mercury's nightside for runs #1–#3, reaching values of over 1000 cm^{-3} (yellow to white regions on the nightside in Figure 2). The MP is associated with a sudden decrease of number density, inward of the BS, dropping to values lower than 10 cm^{-3} (dark blue regions in Figure 2).

In runs #2 and #3, the modeled B_Z component (bottom row of Figure 1) allows to search for possible regions of closed planetary field lines upstream of Mercury. Since the IMF points in the $(+Z)$ direction in run #1, B_Z cannot be used to discriminate between the upstream magnetic field and the planetary dipole above Mercury's dayside apex ($X = 1\ R_M$, $Y = Z = 0\ R_M$). Panel 1(l) shows that for a southward IMF, no positive B_Z component exists upstream of Mercury. In addition, panel 1(c) confirms that no closed magnetic field lines are present sunward of the planet. This finding is consistent with the model results of Guo et al. (2023). The absence of such field lines results in the solar wind density (panels 2(c), (f)) and bulk velocity (not shown here) remaining at its upstream value above Mercury's low-latitude dayside surface. This indicates that no BS is formed sunward of the planet in run #3, meaning that solar wind particles can directly impact onto the surface. Kabin et al. (2000) applied an MHD simulation to model a DDM event at Mercury and similarly found no BS at low latitudes upstream of the planet. In agreement with our results (panels 1 (c), (f) and 2 (c), (f)), the flanks of a parabolic BS are still visible downstream of Mercury in the model output of Kabin et al. (2000). A similar behavior was also identified through observations and modeling at, for example, the Terrestrial moon: the incident plasma impinges directly onto the surface without experiencing prior deceleration, and no BS is formed (Fatemi et al., 2013; Rasca et al., 2021, 2022). The absence of a BS above the low-latitude dayside in run #3 is also supported by observations from the 2013 DDM event. Winslow et al. (2020) identified the BS crossings in MESSENGER magnetometer data from the first orbit, with the dayside crossing located at a near-polar latitude of 70°. They determined the subsolar BS standoff distance to be located below Mercury's surface.

For runs #1 and #2, a BS is still present upstream of Mercury, as indicated by the enhanced proton number density and magnetic field magnitude sunward of the planet (first two rows of Figures 1 and 2). The subsolar standoff distance of the BS decreases from 1.25 R_M in run #1 to 1.08 R_M for run #2. Both these distances are significantly smaller than the average value under nominal solar wind conditions (1.96 R_M; see Winslow et al., 2013). The maximum field strength along the positive X axis decreases by 35% (714 nT vs. 464 nT) from run #1 to run #2 (panels 1(a), (b)). In the low-latitude dayside region, the planetary dipole field points in the $(+Z)$ direction. Therefore, a northward IMF inhibits reconnection while a solar wind field in the $(\pm Y)$ direction can cause reconnection at the dawn and dusk flanks of the magnetosphere (see also Leyser et al., 2017). Hence, we attribute the drop of magnetic field magnitude upstream of Mercury to increased dayside reconnection in run #2 which facilitates the transport of magnetic flux from the dayside to the nightside. Along the positive X axis, the maximum proton number density for run #1 is approximately 1188 cm^{-3} (3.3 times the upstream density) and for run #2 it is 1080 cm^{-3} (3.0 times the upstream density). We ascribe the decrease of the density jump to increased reconnection rates in run #2 compared to run #1. Since the Mach numbers of the solar wind are smaller than at Earth (see Table 1), both density increases are below the maximum value of four permitted by the Rankine-Hugoniot conditions, which is the upper limit at a shock in MHD theory.

A dawn-dusk-asymmetry is visible in the proton number density for $X > 0\ R_M$ in run #3 (panel 2(f)). The density pileup is more pronounced for $Y > 0\ R_M$ (dusk) in the dayside hemisphere than for $Y < 0\ R_M$ (dawn). Such an asymmetry may stem from different reconnection efficiencies in the dawn and dusk hemispheres, resulting in

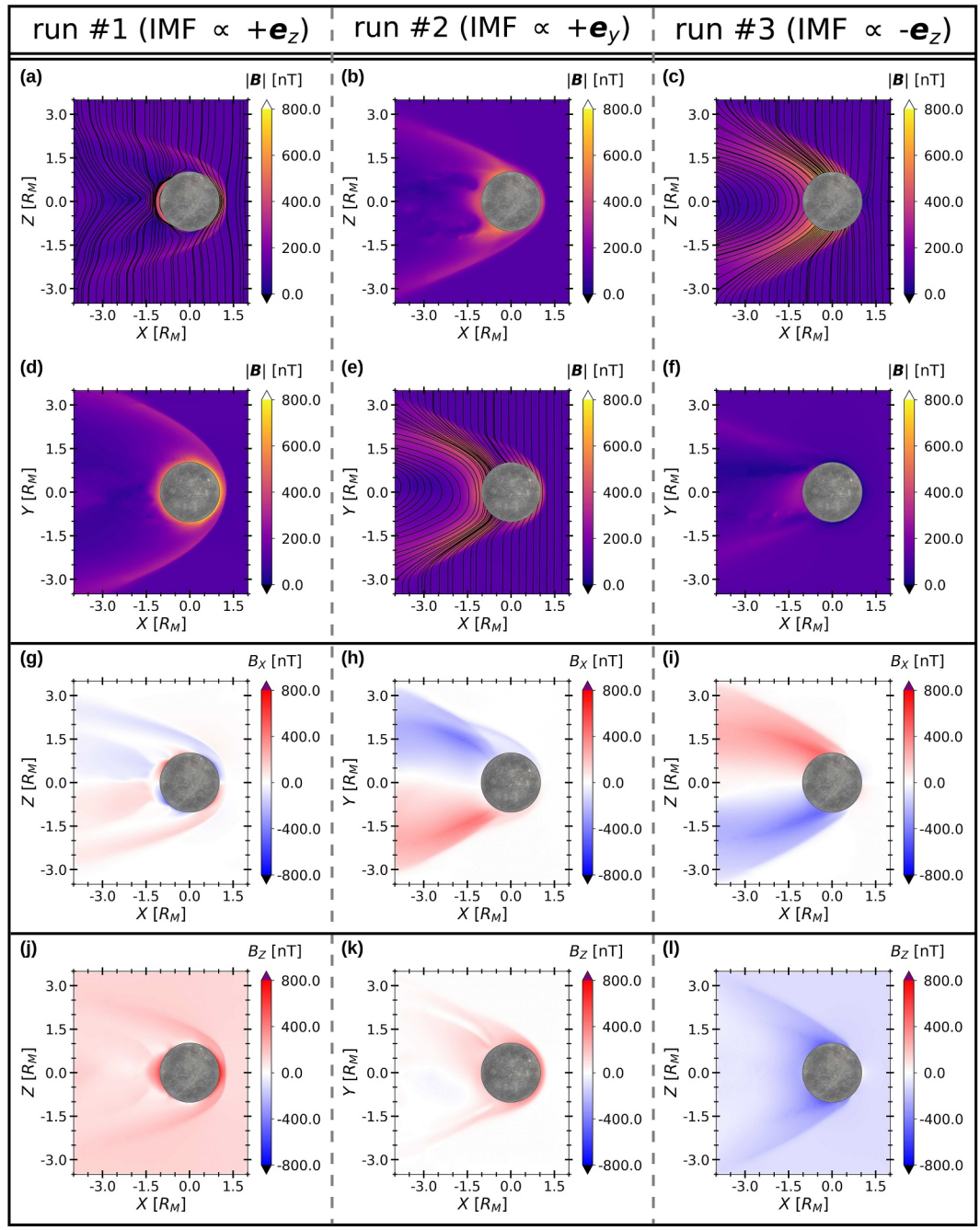

Figure 1. Magnetic field computed with the AIKEF model for runs #1 − #3, using a centered planetary dipole moment. The first column (panels (a), (d), (g), and (j)) depicts model output from run #1 with the IMF pointing in the (+Z) direction, the second column (panels (b), (e), (h), (k)) shows results from run #2 with the IMF oriented in the (+Y) direction, and the third column (panels (c), (f), (i) and (l)) displays run #3 with the IMF in the (−Z) direction. Panels (a)–(f) show the field magnitude, panels (g)–(i) the B_X component, and panels (j)–(l) the B_Z component. The first row displays the $X - Z$-plane (noon-midnight meridian) and the second row the $X - Y$-plane (equatorial). The field components (rows three and four) are depicted in the planes through the center of Mercury containing the IMF vector ($X - Z$-plane for runs #1, #3 and $X - Y$-plane for run #2). Panels (a), (c), and (e) also display the magnetic field lines; these cutting planes are defined by the IMF and the incident solar wind velocity. We do not show field lines in planes that are perpendicular to the upstream field vector. The planet's position is indicated by the image of Mercury.

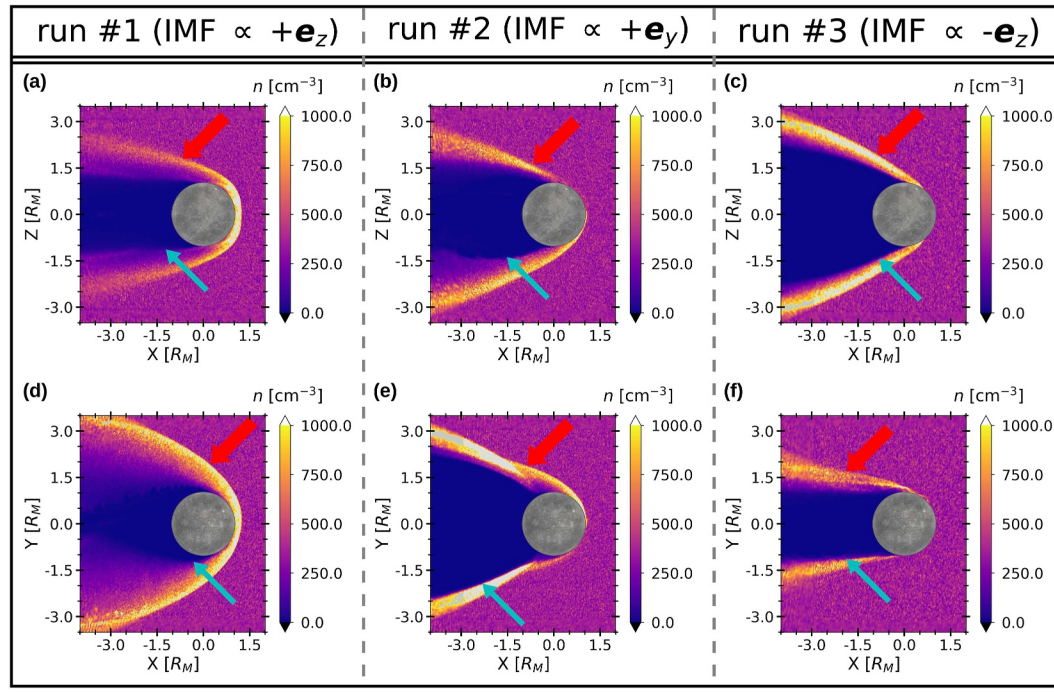

Figure 2. Results for proton number density from the AIKEF model for runs #1 − #3. The first row (panels (a)–(c)) shows the $X - Z$-plane and the second row (panels (d)–(f)) the $X - Y$-plane. The first column displays results from run #1, the second column depicts run #2, and the third column shows run #3. The modeled MP and BS are marked with thin cyan (MP) and bold red arrows (BS).

locally higher erosion rates of the dayside MP. Li et al. (2024) applied an MHD model to emulate the global structure of Mercury's magnetosphere and combined it with a particle-in-cell code to study kinetic signatures and asymmetries associated with reconnection in the dayside magnetosphere. They found that, independent of the IMF orientation, dayside reconnection is more likely to occur on the dawnside than on the duskside. This supports our result that the dayside boundary layer is less pronounced in the dawn hemisphere than in the dusk hemisphere.

As can be seen from the B_X component (third row of Figure 1) a magnetotail is formed downstream of Mercury for runs #1 − #3. Two lobes are visible (red and blue regions on Mercury's nightside in panels 1(g), (h), (i)). The strength and width of the draping signatures gradually increase when the IMF is rotated from $(+\boldsymbol{e}_Z)$ to $(+\boldsymbol{e}_Y)$ and $(-\boldsymbol{e}_Z)$. The maximum magnetic field magnitude in Mercury's nightside magnetosphere ($X < -1.0\ R_M$, first two rows of Figure 1) increases from run #1 (558 nT) to run #2 (580 nT) and run #3 (662 nT); the same trend is visible in the B_X component (run #1: 248 nT; run #2: 439 nT; run #3: 519 nT). We attribute this enhancement to increasing amounts of magnetic flux being transported from Mercury's dayside to the nightside due to reconnection when the field orientation changes in the order $(+\boldsymbol{e}_Z) \rightarrow (+\boldsymbol{e}_Y) \rightarrow (-\boldsymbol{e}_Z)$. Mercury's magnetotail in run #1 retains a small region of closed dipole field lines immediately above the nightside surface (panel 1(a)). The presence of such field lines is qualitatively consistent with MESSENGER observations during DDM events (Slavin et al., 2019; Winslow et al., 2020). However, downstream of approximately $X = -1.5\ R_M$ the signs of the B_X perturbations in the northern and southern hemispheres reverse, switching to $B_X < 0$ nT in the north (blue in panel 1(g)) and $B_X > 0$ nT south of the planet's equator (red). This region is no longer dominated by the stretching of the planetary field toward downstream. Rather, the IMF becomes "bulged" when encountering the downstream side of Mercury's magnetosphere. The same effect was seen in MHD simulations when Earth's magnetosphere is exposed to a northward IMF (Song et al., 2000; Figure 1): the planetary field lines are stretched into a tail only at distances below 60 Earth radii. At larger distances, the "closed" magnetosphere causes draping of the IMF, stretching *anti*-parallel to the Sun-planet line. We note that run #3 does not reveal any closed field lines on Mercury's nightside within the $X - Z$-plane (panel 1(c)). However, this may be a result of the field line tracer's limited resolution.

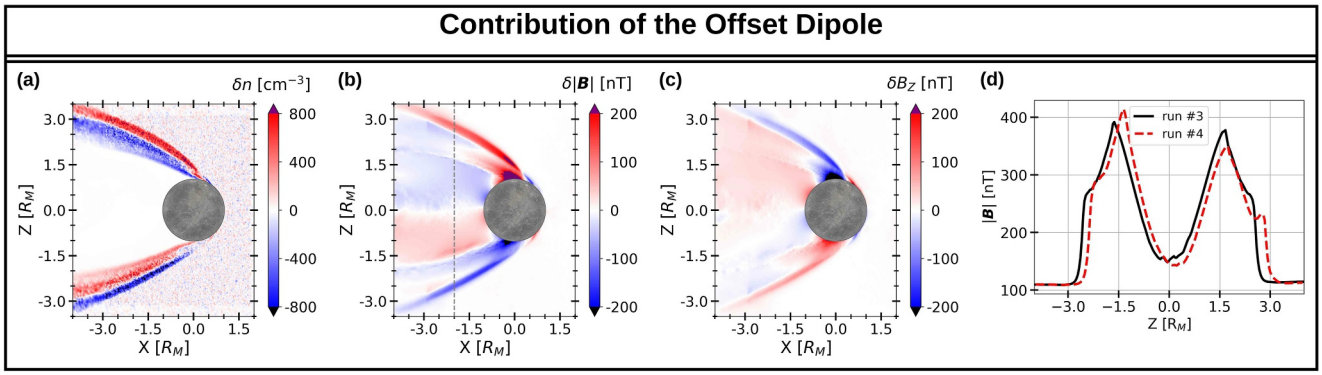

Figure 3. Comparison of model results from runs #4 and #3. Panels (a)–(c) show the difference of several plasma parameters in the $X - Z$-plane between these two runs. For any parameter f we define $\delta f := f_{\#4} - f_{\#3}$, where $f_{\#4}$ represents that parameter for run #4 and $f_{\#3}$ is the quantity from run #3. The panels depict (a) the difference in the proton number density, (b) the magnetic field magnitude, and (c) the B_Z component. In panels (a) and (b), the red hue indicates regions where the value is higher in run #4 compared to run #3, while blue stands for lower values in run #4. White color means that the value in the respective region is the same in both runs. For the interpretation of panel (c), it is important to note that B_Z assumes a negative sign in the entire model domain (see panel 1(l)). Hence, blue shading means that the value of B_Z is lower in run #4, but the magnitude $|B_Z|$ is larger in run #4. Panel (d) shows the magnetic field magnitude from runs #3 and #4 along the straight line at $X = -2\ R_M$ and $Y = 0\ R_M$. The dashed red line displays the results for run #4 and the solid black line represents the model output of run #3. In panel (b), the location of this cut is illustrated by the gray dashed line.

We have performed an additional run (#6) with the solar wind ram pressure from the 2011 DDM event, which is the smallest reported value for such an event so far (Slavin et al., 2019) and almost 70% lower than in run #3. As discussed in Appendix A, this reduction of upstream pressure does not qualitatively impact the physics of Mercury's magnetosphere during a DDM event.

3.2. Contribution of the Offset Dipole

To isolate the influence of the dipole offset on Mercury's plasma environment during a DDM event, panels (a)–(c) of Figure 3 display the difference of several parameters between runs #4 and #3 in the $X - Z$-plane. Panel 3(d) shows the magnetic field magnitude for both runs along the straight line at $X = -2\ R_M$ and $Y = 0\ R_M$. The solar wind conditions are the same for runs #3 and #4. While run #3 applies a centered planetary dipole moment, we include the observed offset toward the north for run #4 (see Table 1).

Panel 2(c) reveals that the proton number density on Mercury's nightside is enhanced along the outer boundary layer of the magnetosphere and is reduced in a broad central area (dark blue region). As can be seen in panel 3(a), this structure is shifted northward, which yields lower density values at the southern flank in run #4 than in run #3 (blue, ray-like region). This displacement toward north also causes a density enhancement in the central tail (red, ray-like region in the southern half space). In the same way, the dipole offset yields a depletion and an enhancement of the density in the northern half space in run #4 compared to run #3 (blue and red regions). The broad white area downstream of Mercury denotes the region where the proton number density is low in both runs (panel 3(a)).

The displacement of Mercury's magnetospheric boundary layers is also visible in the magnetic field on the planet's nightside (panel 3(b)). As can be seen in panel 1(c), the magnetotail consists of two lobes with enhanced field magnitude, as well as a broad region between the lobes with reduced $|\boldsymbol{B}|$. Since the magnetotail in run #4 is shifted to the north, the field magnitude at its southern flank is lower than in run #3 (blue, ray-like region in panel 3(b)). In addition, the southern tail lobe in run #4 reaches into the region of decreased magnetic field magnitude directly downstream of Mercury in run #3, yielding an enhancement of the field strength in that region (red area downstream for $Z < 0\ R_M$). The same effect causes the broad reduction and narrow enhancement of the field magnitude downstream of Mercury in the northern hemisphere (blue and red regions in panel 3(b)).

Compared to run #3, the B_Z component in run #4 is enhanced around the southern edge of the magnetotail (red, ray-like region in panel 3(c)) and decreased in the north (blue, ray-like region). Since the B_Z component is negative in the $Y = 0\ R_M$ plane (see panel 1(l)), the regions of enhanced B_Z in run #4 (red) correspond to a lower absolute value $|B_Z|$ in the respective region, whereas a decreased B_Z component (blue) indicates an enhancement of $|B_Z|$ in run #4. Hence, the absolute value of B_Z in Mercury's nightside magnetosphere is shaped by the same

northward displacement as $|\boldsymbol{B}|$. Panel 3(d) shows that for both runs, the magnetic field magnitudes along the cut at ($X = -2\ R_M, Y = 0\ R_M$) display an M-like pattern that corresponds to the two lobes of the magnetotail (maxima) and the region of reduced field strength in between around $x \approx 0\ R_M$ (minimum). For the offset dipole (run #4), this structure is shifted northward by approximately 0.2 R_M. Neither run #3 nor run #4 reveal any low-latitude dayside structures. To provide additional context, Appendix B displays results analogous to Figure 3, but in the MSM coordinate system. In that frame, the $X - Y$-plane is defined by the magnetic equator.

3.3. Model-Data Comparison for the 2013 DDM Event

3.3.1. Data Description and Model Setups

We now apply AIKEF to support the analysis of magnetometer observations from the 2013 DDM event (Orbit 2577, see Winslow et al., 2020). We point out that, apart from the magnetic field, the incident solar wind conditions (during *all* four DDM events) are not constrained through in situ observations. In particular, there is no information available on any time variability of the solar wind pressure and bulk velocity while MESSENGER resides inside of Mercury's magnetosphere. Therefore, we do not expect the model to match the magnitude and extensions of all the observed magnetic features. Rather, we proceed analogous to a preceding study of Mercury's magnetosphere during an HCM event by Exner et al. (2018): these authors carried out AIKEF runs for multiple sets of steady-state upstream conditions. In this way, they attempted to estimate the contributions of different upstream regimes to the various interaction signatures observed inside of Mercury's magnetosphere. Exner et al. (2018) found that there was no single set of upstream conditions that would explain the signatures observed along different segments of MESSENGER's orbit, and even the selected parameter sets could only partially reproduce the observed time series. This disparity was attributed to the presence of short-scale time variations in the incident flow conditions, not captured by the model. Since a single AIKEF run requires a computing time of about a week, charting more than a small corner of parameter space is infeasible. To provide some context for the observations, we therefore consider a few sets of incident flow conditions that are within the range of estimates from Winslow et al. (2020) and match the observed magnetic field in selected segments of the upstream region.

Panel 4(a) shows in black the observed magnetic field with a resolution of 1 s. To visualize overall trends in the field, the red line displays the time series obtained with a 40 s running average (analogous to Slavin et al., 2019). The spacecraft traveled less than 0.06 R_M during any 40 s segment of orbit 2577. The interval shown in Figure 4a is located within the magnetic cloud of the ICME that caused the 2013 DDM event (Winslow et al., 2020). In this region of an ICME, the magnetic field is usually very smooth and reveals steady rotations over time scales of several hours at Mercury (e.g., Bowers et al., 2025; Burlaga, 1988; Good & Forsyth, 2016; Winslow et al., 2015).

At the beginning of the plotted time series (16:30 UTC on 30 November 2013), MESSENGER was located upstream of Mercury's magnetosphere in the solar wind. Around 16:50 UTC and still sunward of the planet, short-scale fluctuations began to appear in the observed field. These signatures may be associated with, for example, foreshock waves as observed and modeled by Fairfield and Behannon (1976), Le et al. (2013), Jarvinen et al. (2019), or Romanelli and DiBraccio (2021). However, simulating these waves requires an increase in the number of macroparticles per cell by about an order of magnitude, compared to our AIKEF setups. Hence, the simulation runtime would increase significantly, thereby limiting the number of scenarios that we can investigate. Therefore, we have decided against modifying our model to accommodate this aspect of the interaction. In addition to the wave activity, the observed B_Y component reversed its sign from negative to positive around 16:50 UTC. Shortly after 17:15 UTC (light blue time marker) and immediately upstream of Mercury's BS the MESSENGER magnetometer detected an increase of B_Z by about 20 nT, switching signs from negative to positive.

Winslow et al. (2020) identified multiple inbound BS crossings in magnetometer data, with the first one occurring around 17:22 UTC and the last one detected near 17:33 UTC. These transitions are indicated by the sharp increases/decreases of the field magnitude (see also criteria from Winslow et al., 2013). The detection of multiple BS crossings implies that this boundary layer was moving relative to the spacecraft, which constitutes a commonly observed effect at Mercury (e.g., Fairfield & Behannon, 1976; Winslow et al., 2013). MESSENGER's inbound crossing of the MP occurred at approximately 17:36 UTC, characterized by the sudden changes in B_X and B_Z (Winslow et al., 2013, 2020). The spacecraft then entered the nightside segment of the orbit (gray shaded region in panel 4(a)) around 17:37 UTC. The observed crossing of the magnetotail's neutral sheet, defined by $B_X = 0$ nT, occurred around 18:08 UTC. The outbound MP (black arrows in panel 4(a)) was detected at

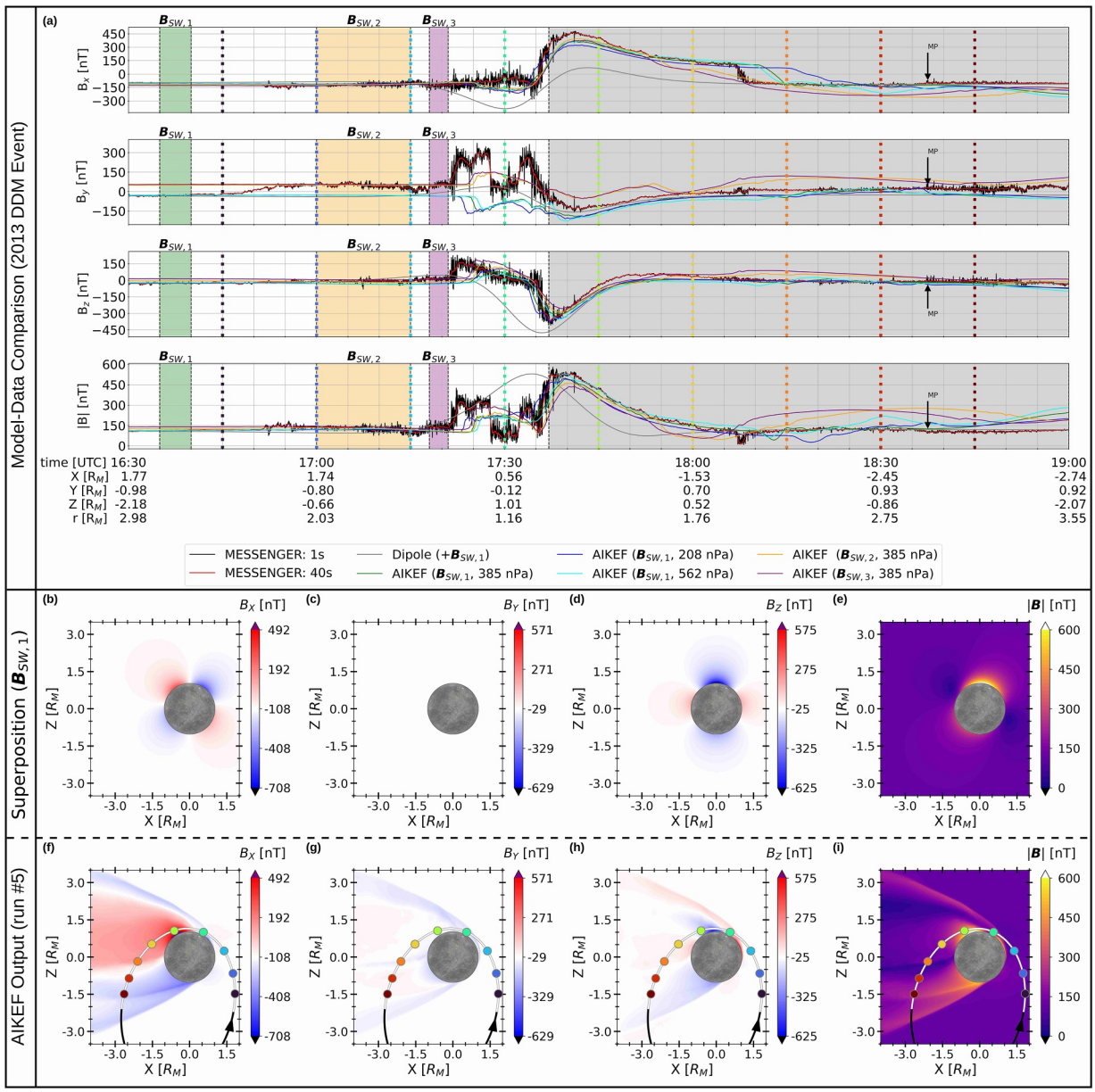

Figure 4. Comparison between AIKEF model results and MESSENGER magnetometer data for the 2013 DDM event (Orbit 2577, Winslow et al., 2020). We show data in the interval from 16:30–19:00 UTC on 30 November 2013. Panel (a) depicts MESSENGER observations and output of several AIKEF runs. From top to bottom, panel (a) shows B_X, B_Y, B_Z, and the field magnitude. The quantity $r = \sqrt{X^2 + Y^2 + Z^2}$ denotes the distance to the origin of the MSO system. The colored segments before 17:30 UTC indicate intervals over which we averaged the observed magnetic field to obtain Interplanetary Magnetic Field (IMF) vectors used as input for the AIKEF runs (green: $\boldsymbol{B}_{SW,1}$, orange: $\boldsymbol{B}_{SW,2}$, purple: $\boldsymbol{B}_{SW,3}$). The gray shaded region marks the nightside section of MESSENGER's orbit and the black arrows shortly after 18:35 UTC (labeled MP) show the observed outbound MP crossing (Winslow et al., 2020). The black lines in panel (a) depict MESSENGER magnetometer data with a 1 s time resolution. Red indicates the data obtained with a 40 s running average (analogous to Slavin et al., 2019). The superposition of Mercury's internal dipole field and $\boldsymbol{B}_{SW,1}$ (without inclusion of plasma effects) is represented by the gray lines. The AIKEF output is depicted in green (run #5: $\boldsymbol{B}_{SW,1}$, with an upstream pressure of 385 nPa), blue ($\boldsymbol{B}_{SW,1}$, with an upstream pressure of 208 nPa), cyan ($\boldsymbol{B}_{SW,1}$, with an upstream pressure of 562 nPa), orange ($\boldsymbol{B}_{SW,2}$, with an upstream pressure of 385 nPa), and purple ($\boldsymbol{B}_{SW,3}$, with an upstream pressure of 385 nPa). The colored dotted lines mark time stamps every 15 min. The vertical gray lines in the background show increments of 5 min. Panels (b)–(e) depict two-dimensional cuts through the magnetic field obtained from superposition of the planet's internal dipole and $\boldsymbol{B}_{SW,1}$. Panels (f)–(i) show the field in Mercury's magnetosphere, as obtained with AIKEF for run #5. Both rows display the model results in the $X - Z$-plane. From left to right, the panels depict B_X (b), (f), B_Y (c), (g), B_Z (d), (h), and the field magnitude (e), (i). For the field components, the color bar is centered around the undisturbed IMF values from run #5 (white). In the bottom row the black/white lines mark the projection of MESSENGER's trajectory during orbit 2577 onto the $X - Z$-plane. The white segment of the orbit is the part shown in panel (a) and the black arrow indicates the direction of travel for the spacecraft. The colored dots along the trajectory correspond to the time markers (vertical dashed lines) of the same colors in panel (a).

approximately 18:37 UTC, indicated by the increased amplitude of magnetic fluctuations (Winslow et al., 2013, 2020). The outbound crossing of the BS was encountered around 21:00 UTC south of Mercury and in the downstream hemisphere. This event is not displayed in panel 4(a).

MESSENGER observed several different magnetic field regimes upstream of the initial BS crossing at 17:22 UTC. Analogous to Exner et al. (2018), we therefore carried out multiple AIKEF runs, each of them applying an averaged IMF vector from a different segment of the trajectory (colored regions in panel 4(a)). Before 16:50 UTC, the IMF observed sunward of Mercury's magnetosphere was nearly uniform and we used the interval from 16:35 UTC until 16:40 UTC (green region in panel 4(a)) to calculate an averaged field vector of $\boldsymbol{B}_{SW,1} = (-108,\ -29,\ -25)$ nT. For the segment with positive B_Y (starting around 16:50 UTC), we considered the interval from 17:00 UTC to 17:15 UTC (orange region) and obtained $\boldsymbol{B}_{SW,2} = (-116, 47,\ -9)$ nT. To obtain an averaged field in the region immediately upstream of the BS with positive B_Z, we applied the interval from 17:18 UTC until 17:21 UTC (purple region), yielding $\boldsymbol{B}_{SW,3} = (-127, 53, 11)$ nT. The magnitudes of these three IMF vectors read $|\boldsymbol{B}_{SW,1}| = 115$ nT, $|\boldsymbol{B}_{SW,2}| = 125$ nT, and $|\boldsymbol{B}_{SW,3}| = 138$ nT. The vectors $\boldsymbol{B}_{SW,2}$ and $\boldsymbol{B}_{SW,3}$ are inclined against $\boldsymbol{B}_{SW,1}$ by 38° and 41°, respectively. We investigate the influence of these three IMF vectors on the structure of the magnetosphere.

We carried out three AIKEF runs using the IMF vectors $\boldsymbol{B}_{SW,1}$, $\boldsymbol{B}_{SW,2}$, and $\boldsymbol{B}_{SW,3}$, combined with a ram pressure of 385 nPa. Winslow et al. (2020) suggest an uncertainty of ±177nPa for this value. We selected the undisturbed IMF, upstream of Mercury ($\boldsymbol{B}_{SW,1}$), which is not affected by foreshock structures and the mean pressure of 385 nPa as our baseline run (setup #5 in Table 1). In addition, we performed two runs with upstream pressures of $(385 - 177)$ nPa = 208 nPa and $(385 + 177)$ nPa = 562 nPa for this IMF vector. The solar wind pressure in these runs was adjusted by modifying the upstream proton density while keeping the bulk velocity at $u_{SW} = 800$ km s^{-1} (see run #5 in Table 1). For all five setups the solar wind is supermagnetosonic, with M_A in the range from 4.5 to 7.4 and M_{MS} from 4.1 to 5.9. The modeled time series from these five runs as well as a mere superposition of Mercury's internal dipole field and $\boldsymbol{B}_{SW,1}$ (i.e., without plasma effects) are shown in panel 4(a). This superposition setup is included to provide guidance for the identification of regions where the planet's internal field experiences strong deformation by the solar wind interaction. Panels 4(b)–(e) display the field from the superposition scenario in the $X - Z$-plane and panels 4(f)–(i) show the AIKEF results from run #5 in this plane. The color bars in panels 4(b)–(d) and panels 4(f)–(h) are centered around the IMF values (white). We emphasize that the color bars in panels 4(b) and (f) are *not* centered around $B_X = 0$ nT, which would reveal the location of the neutral sheet in Mercury's magnetotail. The identification of this region is facilitated by additional illustrations in Figure 5 that will be discussed later. The $X - Z$-plane is tilted against the plane containing MESSENGER's orbit by less than 25°. The spacecraft's orbital plane is centered around the origin of the MSO system. Hence, the two-dimensional cuts in panels 4(f)–(i) do not precisely coincide with MESSENGER's orbital plane, but they are still suitable to contextualize the interpretation of the magnetic signatures observed along the trajectory.

3.3.2. Model-Data Comparison: B_X Component

The top row of panel 4(a) displays the modeled and observed B_X components. Around 17:25 UTC (shortly before the turquoise time marker) the B_X values in all five AIKEF runs decrease, with the minima being 55 nT to 105 nT lower than B_X in the undisturbed solar wind. Panel 4(f) reveals a region of reduced B_X at the northern flank of Mercury's magnetosphere (blue hue), corresponding to the BS. The turquoise time marker confirms that the modeled B_X signature around 17:25 UTC is caused by the trajectory intersecting this boundary layer. Panel 4(b) shows that the superposition of Mercury's dipole and the IMF already results in a decreased B_X component in the northern upstream quadrant ($X > 0\ R_M,\ Z > 0\ R_M$, blue hue). Therefore, the observed increase in B_X can neither be associated with the undisturbed IMF nor the internal dipole which both have negative B_X components in this segment of the trajectory. The increased B_X observed by MESSENGER before 17:36 UTC could be caused by draping of the IMF within Mercury's magnetosheath around the planet's magnetosphere. The orientation in such a draping signature strongly depends on the IMF orientation (see also Zhong & Wang, 2024). Since none of our three chosen IMF vectors can explain the B_X enhancement observed around 17:30 UTC, the field vector that shaped Mercury's magnetosphere along this segment of the trajectory may have been different from the ones used as input for our model runs. Alternatively, the observed signature may be caused by dynamically changing solar wind conditions while AIKEF applies constant upstream flow parameters.

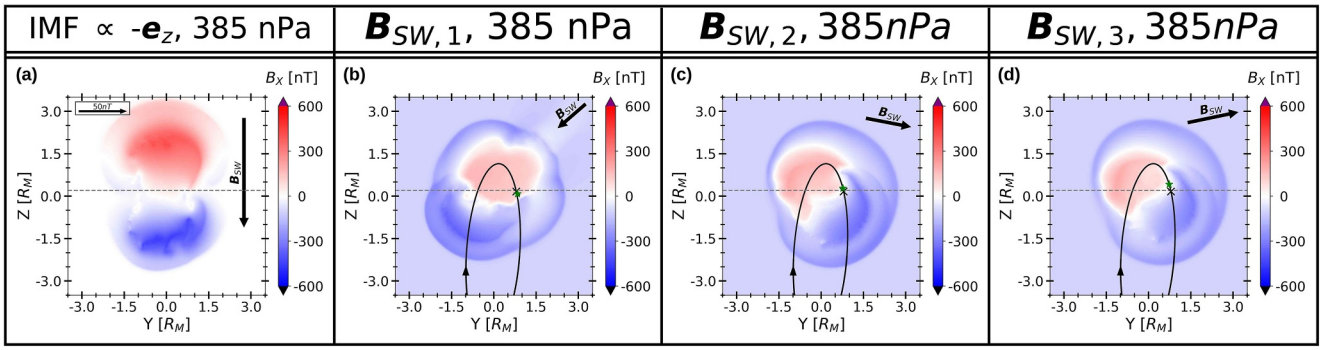

Figure 5. Modeled B_X component in the magnetotail, taken from different AIKEF runs in the plane perpendicular to the Sun-Mercury line at $X = -1.86\ R_M$. Panel (a) shows results from run #4 with the IMF pointing in $(-Z)$ direction, panel (b) depicts model output from run #5 applying $\boldsymbol{B}_{SW,1}$, panel (c) displays results from the run using $\boldsymbol{B}_{SW,2}$, and panel (d) shows the output from the run with $\boldsymbol{B}_{SW,3}$. All four runs use an upstream ram pressure of 385 nPa (see Winslow et al., 2020). In panels (b), (c), and (d) the black cross marks the position of the observed neutral sheet crossing (along MESSENGER's trajectory), which is located within the $X = -1.86\ R_M$ plane. The green asterisks depict the modeled crossings from the respective AIKEF runs, projected onto the cutting plane. The dashed gray line indicates the magnetic equator of Mercury's dipole field at $Z = 0.2\ R_M$. The black line in panels (b)–(d) depicts the projection of MESSENGER's orbit into the $X = -1.86\ R_M$ plane, with the arrow indicating the direction of travel. The arrow, labeled $\boldsymbol{B}_{SW}$, in the upper right corner of each panel displays the orientation of the respective IMF vector projected onto the cutting plane (0, B_Y, B_Z). The length of these vectors represents the magnitude of the projected field $\sqrt{B_Y^2 + B_Z^2}$. In the upper left corner of panel (a) the black arrow indicates the scale for the visualization of the IMF vectors.

Around 17:36 UTC, the MESSENGER spacecraft crossed the inbound MP (see also Winslow et al., 2020). In this segment of the trajectory, the observed B_X sharply increases and turns positive, reaching a maximum value of $B_X = 462$ nT at 17:41 UTC. This increase is visible in all five AIKEF runs. However, the modeled increase is more gradual than observed. The locations of the modeled and observed B_X maxima are displaced against each other by less than 0.2 R_M, and the peak values in the AIKEF results remain $(15 - 30)\%$ below the observed one. The smallest deviation between the observed and modeled maximum value occurs in the run using $\boldsymbol{B}_{SW,2}$ (orange line). Panels 4 (b) and (f) show that the observed increase in B_X is associated with the spacecraft's passage through the northern magnetotail lobe. While the planetary dipole field alone already causes an enhancement of B_X in this region (red in panel 4(b)), the observed maximum value exceeds the one from the superposition case by a factor of 5 (gray line in panel 4(a)). This implies that the stretching of the planetary field lines by plasma effects is needed to explain the observed B_X signature.

During the passage through the northern magnetotail lobe (approximately 17:40 UTC–18:05 UTC), both the modeled and the observed B_X component gradually decrease. After 17:50 UTC the magnetic field profile from the run applying the enhanced upstream pressure and $\boldsymbol{B}_{SW,1}$ (cyan lines in panel 4(a)) quantitatively matches the observed B_X. The time series sampled by MESSENGER suggests that the spacecraft crossed the neutral sheet of Mercury's magnetotail (indicated by $B_X = 0$ nT) around 18:08 UTC and at $Z = 0.17\ R_M$, that is, south of the planet's magnetic equator ($Z = 0.20\ R_M$). For the runs using $\boldsymbol{B}_{SW,1}$ (green, blue, and cyan lines in panel 4(a)), the positions of the modeled neutral sheet crossings range from $Z = -0.32\ R_M$ to $Z = -0.03\ R_M$; that is, these occur below $Z = 0.2\ R_M$ and qualitatively agree with the observed southward displacement. The smallest deviation between the locations of the modeled and observed crossings is achieved with the run applying the enhanced upstream pressure (cyan lines). In the runs applying $\boldsymbol{B}_{SW,2}$ (orange lines) and $\boldsymbol{B}_{SW,3}$ (purple lines), the neutral sheet crossings occur earlier in time (18:05 UTC and 18:02 UTC, respectively) and north of Mercury's magnetic equator at $Z = 0.28\ R_M$ ($\boldsymbol{B}_{SW,2}$) and $Z = 0.42\ R_M$ ($\boldsymbol{B}_{SW,3}$). This indicates that the IMF orientation plays an important role in shaping the neutral sheet.

To explain the dependence of the modeled neutral sheet crossings on the IMF orientation, Figure 5 shows the B_X component from several AIKEF runs for the plane perpendicular to the Sun-Mercury line at $X = -1.86\ R_M$. This plane contains the observed neutral sheet crossing at position $(X, Y, Z) = (-1.86, 0.80, 0.17)\ R_M$. In Figure 5, the color bars are centered around $B_X = 0$ nT; that is, the white regions between the tail lobes (red and blue) indicate the neutral sheet (this is *not* the case in Figure 4). Panel 5(a) shows AIKEF results for run #4, with the IMF pointing in $(-Z)$ direction; in other words, the B_Y component of the IMF is zero in this run. The red and blue regions indicate the northern and southern tail lobes, and the neutral sheet approximately coincides with the magnetic equator of the planetary dipole (dashed gray line). Panel 5(b) shows the results for run #5, with B_Y being

negative in the solar wind. Panel 5(c) displays output from the run using $\boldsymbol{B}_{SW,2}$, and panel 5(d) depicts output from the run applying $\boldsymbol{B}_{SW,3}$. Both $\boldsymbol{B}_{SW,2}$ and $\boldsymbol{B}_{SW,3}$ possess a positive B_Y component. For run #5 the magnetotail is rotated clockwise around a straight line parallel to the negative X axis and going through the center of Mercury's dipole field (panel 5(b)). When applying $\boldsymbol{B}_{SW,2}$ or $\boldsymbol{B}_{SW,3}$, the rotation is anticlockwise (panel 5 (c) and (d)). This rotation causes the modeled neutral sheet crossing along the trajectory (green asterisk) to be displaced southward in run #5 and northward in the runs using $\boldsymbol{B}_{SW,2}$, and $\boldsymbol{B}_{SW,3}$, compared to the position of Mercury's magnetic equator (gray dashed line).

Such a rotation of the magnetotail, called tail twisting, has been identified through a statistical analysis of MESSENGER magnetometer data by Romanelli et al. (2022). These authors used observations from the entire orbital phase and found the magnetotail to be twisted clockwise (counterclockwise) for a negative (positive) B_Y component of the IMF. Sun, Slavin, Dewey, et al. (2020) analyzed the observed twisting of Mercury's tail during a single ICME event in 2011 and identified the same behavior: the $B_Y > 0$ nT component of the IMF led to a counterclockwise rotation. This observed dependence is in qualitative agreement with our model results (panels 5 (b)–(d)). Hence, the agreement between the AIKEF runs applying $\boldsymbol{B}_{SW,1}$ and the observed neutral sheet location suggests that the southward displacement (compared to the magnetic equator) can be explained through magnetotail twisting. In addition, the observed orientation of the twisting requires the IMF to have a negative B_Y component (Romanelli et al., 2022), that is, $\boldsymbol{B}_{SW,2}$ and $\boldsymbol{B}_{SW,3}$ are not suitable to explain the location of the neutral sheet crossing seen by MESSENGER.

Winslow et al. (2020) suggested a different mechanism that could cause the neutral sheet crossing to be displaced against Mercury's magnetic equator during the 2013 DDM event. These authors proposed that inclining the velocity vector of the incident solar wind southward by 5° may be suitable to explain this observation. Therefore, we performed an additional AIKEF run using the IMF and ram pressure from run #5 and the inclined solar wind velocity proposed by Winslow et al. (2020). However, in this setup (not shown in Figure 4) the modeled neutral sheet crossing occurred even farther south at $Z = -0.45\ R_M$, compared to $Z = -0.08\ R_M$ for run #5. Hence, a simultaneous occurrence of tail twisting and tilting is not consistent with MESSENGER observations from the 2013 DDM event. Instead, the AIKEF results indicate that tail twisting alone caused the displacement of the observed neutral sheet crossing.

After 18:10 UTC (shortly before the orange time marker in Figure 4) MESSENGER's orbit was located in the southern magnetotail lobe. For this segment of the trajectory, the runs using $\boldsymbol{B}_{SW,2}$ (orange lines in panel 4(a)) and $\boldsymbol{B}_{SW,3}$ (purple lines) suggest B_X values more than 100 nT lower than observed while the time series for the runs applying $\boldsymbol{B}_{SW,1}$ (green, blue, and cyan lines) deviate by less than 80 nT from the observed signature. This is consistent with our findings for the neutral sheet crossing: only the runs using $\boldsymbol{B}_{SW,1}$ could explain the southward shift of that structure. In addition, run #5 (green lines) matches the observations best in the southern lobe, while the setup using the enhanced pressure (cyan lines) reveals up to 50 nT lower B_X values. This suggests that the southern magnetotail lobe was shaped by a smaller upstream pressure than the northern lobe, which is in agreement with findings from Slavin et al. (2019). These authors reported a pressure of 182 nPa for the subsequent orbit (2578), which is 13% smaller than the 208 nPa at the lower end of the range from Winslow et al. (2020). We performed an additional run using the ram pressure reported by Slavin et al. (2019) and $\boldsymbol{B}_{SW,1}$. The results for this run are not shown in Figure 4: the B_X signature deviated by less than 10 nT from the run using the ram pressure of 208 nPa (blue lines in panel 4(a)), supporting the idea that the upstream pressure dropped while MESSENGER was inside of Mercury's magnetosphere.

3.3.3. Model-Data Comparison: B_y Component

The second row of panel 4(a) depicts the modeled and observed B_Y components. At 17:22 UTC the MESSENGER spacecraft detected a sharp increase of B_Y by approximately a factor of six, indicating the first of several BS crossings seen along this orbit. Around 17:28 UTC, the BS was compressed toward the planet, again exposing the spacecraft to the unshocked solar wind and going along with a decrease in B_Y to the IMF value. The final BS crossing was encountered around 17:33 UTC. Since this motion of the BS likely stems from short-scale fluctuations in the upstream conditions, it does not appear in the AIKEF output. All five model runs show an increase in the *magnitude* of B_Y between 17:20 UTC and 17:30 UTC. For $\boldsymbol{B}_{SW,1}$ the B_Y component is negative in the upstream solar wind and becomes even more negative during this segment of the orbit (green, blue, and cyan lines in panel 4(a)). On the other hand, B_Y is positive for $\boldsymbol{B}_{SW,2}$ and $\boldsymbol{B}_{SW,3}$. These two IMF vectors both generate a

B_Y enhancement in the region where MESSENGER sampled the BS crossings (orange and purple lines). This may indicate that the observed BS signature was shaped by an IMF with a positive B_Y. However, the modeled increase of B_Y remains at least two times weaker than the observed one in both runs.

Mercury's internal dipole is anti-aligned with the Z axis and therefore its field vectors do not possess a B_Y component in the $X - Z$-plane. Hence, the superposition scenario merely displays the B_Y component of the IMF in this plane (white in panel 4(c)). A parabolic region of reduced B_Y is formed along the outer flanks of the magnetosphere (blue hue in panel 4(g)), indicating Mercury's BS. The modification of B_Y in the modeled time series stems from the trajectory crossing this boundary layer (turquoise time marker). The increases of $|B_Y|$ in panel 4(a) occur at slightly different times for all five AIKEF runs, indicating that the position of the BS is impacted by the upstream conditions. MESSENGER magnetometer data of the entire orbital phase showed that Mercury's BS is located closer to the planet for higher Alfvénic Mach numbers while it is farther upstream for lower M_A (Pump et al., 2025; Winslow et al., 2013). In agreement with these observations, the BS crossing in the AIKEF output occurs first, that is, farthest upstream ($X = 1.02\ R_M$) for the run with the lowest Alfvénic Mach number of $M_A = 4.5$ (applying the reduced ram pressure and $\boldsymbol{B}_{SW,1}$; blue lines in panel 4(a)). The run with the highest value of $M_A = 7.4$ (using the enhanced pressure and $\boldsymbol{B}_{SW,1}$; cyan lines) results in the BS encounter at the latest point in time, in other words it is located closest to Mercury's surface ($X = 0.83\ R_M$). These findings suggest that the motion of the BS, resulting in several encounters by MESSENGER, may have been caused by a changing Alfvénic Mach number in the solar wind.

From 17:34 UTC onward, the observed B_Y decreases and turns negative, reaching a minimum value of about -135 nT in the northern magnetotail lobe. Afterward, B_Y gradually increases until the neutral sheet crossing around 18:08 UTC. All five AIKEF runs qualitatively match this pattern. During the entire passage through the northern magnetotail lobe the runs applying $\boldsymbol{B}_{SW,1}$ reveal lower B_Y values than observed, with minimum values between -190 nT and -225 nT. In contrast, the runs using $\boldsymbol{B}_{SW,2}$ and $\boldsymbol{B}_{SW,3}$ produce larger values than seen by MESSENGER, resulting in minima of about -54 nT. Since the magnitude of the observed B_Y minimum is between the ones modeled for the different IMF orientations, Mercury's northern tail lobe may have been shaped by the interaction with an IMF vector that slightly deviates from those in our chosen setups.

In the southern magnetotail lobe (after 18:10 UTC) the observed B_Y component remained nearly constant around 0 nT. This region of "flat" B_Y can be seen in all modeled time series between 18:25 UTC and 18:40 UTC. However, only the runs applying $\boldsymbol{B}_{SW,1}$ quantitatively match the observations. Hence, the signatures of the southern lobe in both B_X and B_Y are consistent with an upstream field close to $\boldsymbol{B}_{SW,1}$. Our findings for B_Y suggest that the IMF vector changed during MESSENGER's passage through Mercury's magnetosphere. While the outer dayside region of the magnetosphere may have been shaped by an IMF possessing a positive B_Y component, the southern lobe reveals signatures of an interaction with an IMF vector similar to $\boldsymbol{B}_{SW,1}$ (having a negative B_Y component).

3.3.4. Model-Data Comparison: B_Z Component

The third row of panel 4(a) shows the modeled and observed B_Z components. At 17:22 UTC, when MESSENGER encountered the BS for the first time, the magnetometer detected a sharp increase of B_Z, reaching values of up to 160 nT. Subsequently, this component decreases almost linearly and the 40s average (red lines in panel 4(a)) turns negative before the MP encounter around 17:36 UTC. The observed crossing of the MP is characterized by a sharp decrease of B_Z, resulting in a minimum value of about -380 nT. All five AIKEF runs show an increase of B_Z between 17:20 UTC and 17:30 UTC, with maxima between 55 nT and 185 nT. Consistent with the observations, this enhancement corresponds to the passage through the parabolic BS (red hue near turquoise time marker in panel 4(h)). Downstream of the BS, the B_Z values in all AIKEF runs gradually decrease. Between 17:33 UTC and 17:35 UTC the modeled decrease becomes slightly steeper for all runs, indicating the MP encounter. The modeled MP passage occurred at northern latitudes of 73°–81°, which is slightly south of the observed crossing at 84°.

Panel 4(d) shows that a region of reduced B_Z is already present north of Mercury (blue hue) for the superposition of the planetary dipole and the IMF. The interaction with the incident solar wind stretches this feature toward downstream, thereby forming the northern magnetotail lobe (panel 4(h)). During the passage through this region (nightside segment before the orange time marker), the observed B_Z component (red line in panel 4(a)) gradually increases, reaching positive values around 17:46 UTC. In the southern lobe (after 18:10 UTC) this component

stays nearly constant around 0 nT. While the time series from the five AIKEF runs can qualitatively reproduce the increase seen in the northern lobe, the modeled values of B_Z are lower than observed. Consistent with our analysis of the B_Y component, this again indicates that the field sampled by MESSENGER in this segment of the orbit may have been shaped by the interaction with an IMF vector that slightly deviates from those in our chosen setups. In the southern lobe between 18:10 UTC and 18:45 UTC, all five runs largely reproduce the observed, constant B_Z signature, with the setups applying $\boldsymbol{B}_{SW,1}$ quantitatively matching the value sampled by MESSENGER. In agreement with our results for the B_X and B_Y components, this supports the idea that the southern magnetotail lobe was shaped by an IMF vector similar to $\boldsymbol{B}_{SW,1}$.

3.3.5. Model-Data Comparison: Magnetic Field Magnitude

The bottom row of panel 4(a) presents the absolute value of the observed and modeled magnetic field. The BS encounters detected after 17:22 UTC result in a sequence of sharp increases and decreases of the field magnitude. For all AIKEF runs a single increase, located between the observed ones, is visible in the time series. Since we apply stationary upstream conditions, we do not expect the modeled time series to replicate the observed, dynamic feature of multiple BS crossings: these signatures are likely caused by time-dependent upstream conditions. The run applying $\boldsymbol{B}_{SW,3}$ matches the magnitude of the increase best. In agreement with our findings for the B_Y component, this suggests that the observed BS signature was likely formed through the interaction with an IMF possessing a positive B_Y component. Panel 4(e) shows that the superposition of Mercury's dipole and the IMF already causes an enhanced $|\boldsymbol{B}|$ in the northern upstream quadrant ($X > 0\ R_M$, $Z > 0\ R_M$). The incident solar wind compresses this region toward the planet (panel 4(i)), resulting in the formation of the BS (orange arc north of Mercury).

Around 17:36 UTC the observed field sharply increases, reaching maximum values larger than 500 nT and indicating MESSENGER's crossing of the MP. All AIKEF runs show a gradual increase of $|\boldsymbol{B}|$ in this segment of the orbit. During the subsequent passage through the northern magnetotail lobe, the field magnitude seen by MESSENGER steadily decreases until the neutral sheet crossing around 18:08 UTC. The AIKEF runs produce this pattern as well. The observed neutral sheet crossing is indicated by a narrow dip in $|\boldsymbol{B}|$ around 18:08 UTC. Such a region of reduced field magnitude can be seen in the AIKEF output, but its width, depth, and location strongly depend on the upstream conditions. The modeled time series from the run using $\boldsymbol{B}_{SW,1}$ and the enhanced upstream pressure (cyan lines) matches the observed signature best, again suggesting that the IMF vector changed compared to the one that shaped the BS. In the southern lobe (after 18:10 UTC) the observed $|\boldsymbol{B}|$ signature is almost constant. The runs using $\boldsymbol{B}_{SW,1}$ (green, blue, and cyan lines in panel 4(a)) produce values closer to the ones seen by MESSENGER than the other two setups. The best match is achieved for run #5 (green lines). In agreement with our findings for the B_X component, the field magnitude in this segment of the orbit indicates that in addition to the change of the IMF vector, the upstream pressure also dropped while MESSENGER completed orbit 2577.

We also modeled Mercury's plasma environment during the 2011 DDM event: this was the only one where the upstream magnetic field remained nearly constant on time scales of several hours before MESSENGER's ingress into and after the spacecraft's egress from Mercury's magnetosphere (Slavin et al., 2019). However, analogous to the 2013 event we could not identify a single set (or a narrow range) of upstream conditions that would be able to explain magnetometer observations along the entire orbit. Thus, while comparison to a set of AIKEF runs can provide context for magnetometer observations in selected segments of MESSENGER's orbit, persistent monitoring of the upstream conditions is imperative to develop a (possibly time-dependent) model that can more accurately reproduce data collected during DDM events.

3.4. Plasma Transport Through Mercury's Magnetosphere

We now investigate how the transport of plasma through Mercury's magnetosphere operates during DDM events. For this purpose, we study the time evolution of a "slice" of solar wind protons that interact with the planet's electromagnetic environment. Under nominal solar wind conditions at Mercury, a northward orientation of the IMF inhibits the formation of a Dungey cycle (Slavin et al., 2021), while a southward IMF allows it to occur. The Dungey cycle at Mercury takes about 2–3 min to complete (Slavin et al., 2009, 2010), and the Near Mercury Neutral Line (NMNL) is located at $|X| < 3\ R_M$ for nominal solar wind conditions (Poh et al., 2017).

We considered the fields from runs #1 and #3, both using a centered planetary dipole moment. As discussed in Section 3.2, Mercury's offset dipole only has minor quantitative effects on the structure of the planet's magnetosphere during DDM events. Run #1 uses an IMF oriented antiparallel to Mercury's dipole moment, and for run #3 the IMF and planetary magnetic moment are parallel (see Table 1). We do not include run #2 in this discussion: an IMF orientation perpendicular to Mercury's dipole moment allows reconnection mostly at the dawn and dusk flanks of the magnetosphere (Leyser et al., 2017; Li et al., 2024). Hence, the plasma flow follows a more complex three-dimensional pattern that complicates straightforward access to the involved physics (see also Massetti et al., 2003).

After runs #1 and #3 have reached the quasi-stationary state from Section 3.1, we mark a cuboid-like "slice" of solar wind protons that enter the simulation box at its upstream face ($X = 4\ R_M$) and trace their dynamics as they travel through Mercury's compressed magnetosphere. The initial volume of this slice is set to $0.25\ R_M \times 10\ R_M \times 10\ R_M$, where the extensions in the Y and Z directions are the same as those of the AIKEF domain. Similar to a flip book, Figures 6 and 7 show the time evolution of the number density as well as the magnitude and components of the bulk velocity for the traced particle population. The time increment between consecutive snapshots $t_1, \ldots, t_4$ is set to 6 s, which corresponds to the undisturbed solar wind traveling 2 R_M toward downstream. The traced slice of protons enters the simulation box with a number density of $n_0 = 10^{-10} n_{SW} = 3.6 \cdot 10^{-8}$ cm^{-3} and a bulk velocity of $(u_X, u_Y, u_Z) = (-800, 0, 0)$ km s^{-1} (see Table 1). Due to their low number density, the protons within the slice can be treated as test particles; that is, the currents carried by them are too weak to affect the electromagnetic fields near Mercury. For this reason, only the equations of motion for the protons but not the equations for the electromagnetic fields need to be solved by AIKEF, reducing the required computational time by about 50%. We show results in the $X - Z$-plane which contains the planetary dipole moment, the IMF vector, and the upstream flow direction. The first snapshot of the flip-book ($t_1 = 0$ s) is taken at the point in time when the slice reaches Mercury's dayside apex. The same method of studying magnetospheric dynamics has already been applied with AIKEF to investigate the origin of the "double MP" observed during MESSENGER's first and second Mercury flyby (Müller et al., 2012).

For nominal solar wind conditions, the upstream plasma is decelerated at the BS upstream of Mercury and the slice would then bend around the MP (see Müller et al., 2012). Under DDM conditions, this process can still be seen for a northward IMF (panel 6(a)). For this setup, panels 6(i) and 7(a) show that the traced particles are decelerated by more than 400 km s^{-1} (blue hue sunward of the planet) at the BS. In contrast, panel 6(e) reveals that for a southward IMF the particles impact onto Mercury's low-latitude dayside surface without any prior deflection (panel 7(m)). In this case, no BS exists sunward of the planet (Section 3.1) and the bulk velocity of the traced protons remains unchanged upstream of Mercury (panels 6(m) and 7(e)).

At $t_2 = 6$ s the traced protons in both runs travel north and south of Mercury's disk. For run #1 (northward IMF), these particles cross the BS but cannot penetrate the MP, analogous to the behavior under nominal solar wind conditions. At $t_3 = 12$ s some of the protons spread out into two dilute "clouds" above and below the planet (panel 6(c)), which subsequently "fray out" along the north-south direction (panel 6(d)). In Figure 8 we show the time evolution of the velocity distributions for the $(-v_X)$ and v_Z components within the northern cloud, with $\boldsymbol{v} = (v_X, v_Y, v_Z)$ being the velocity of an individual proton.

The snapshots are taken at the same points in time $t_1, \ldots, t_4$ as used in Figures 6 and 7. In each case, all protons inside of a cuboid-like box (cyan) are considered. At t_1 (when the clouds have not yet formed), we sample the distribution of protons within the undisturbed solar wind to establish a baseline for the following analysis. At the subsequent time steps (t_2, t_3, and t_4), we adapted the volume and location of these cuboids to cover the downstream motion and changing shape of the northern particle cloud. The number of macroparticles inside the selected volumes exceeds 1,000 for all snapshots, suggesting that the sample size is large enough for meaningful statistics. For both velocity components, we plot histograms with bin widths of 50 km s^{-1}. Since the two proton clouds above and below Mercury are nearly symmetric, we focus on the northern one.

Before interacting with Mercury's electromagnetic environment (t_1), the undisturbed solar wind ions show a drifting Maxwellian distribution, centered around $(-v_X) = 800$ km s^{-1} and $v_Z = 0$ km s^{-1} (panels 8(e) and 8(i)). The thermal velocity of the protons $\left(\sqrt{2\ k_B\ T_{SW}\ m_p^{-1}} = 57 \text{ km s}^{-1}\right)$, calculated from the parameters in Table 1, is in agreement with the width of the distributions in panels 8(e) and 8(i). When the protons cross the

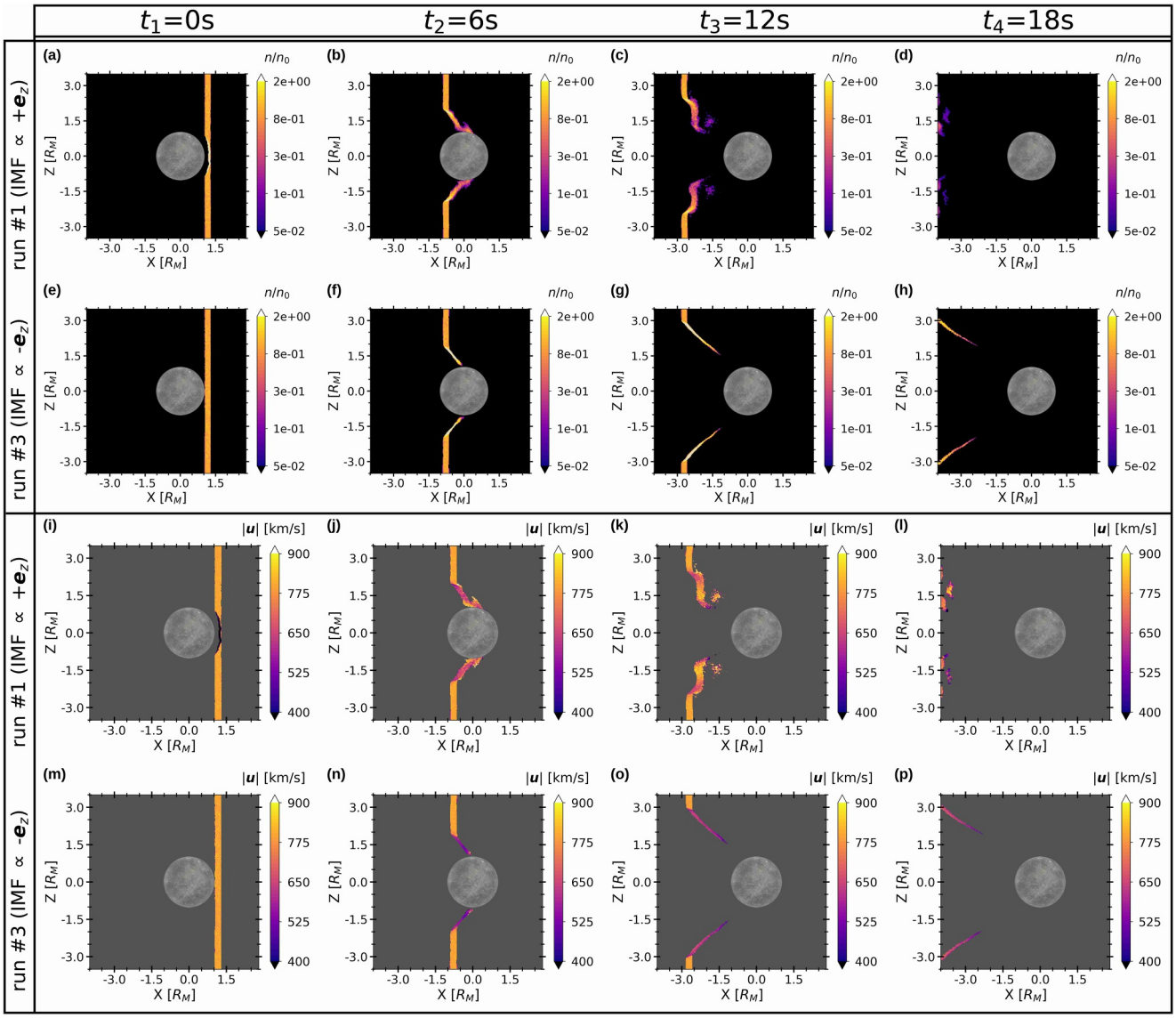

Figure 6. Real-time tracing of a "slice" of solar wind protons in the $X - Z$-plane. The figure shows snapshots at several points in time for the number density and bulk velocity of the traced particle populations from runs #1 and #3. The top row (panels (a)–(d)) depicts the modeled number density for run #1 with the IMF pointing northward, and the second row (panels (e)–(h)) displays the density from run #3 where the IMF is oriented southward. The density is normalized to the value of the proton slice in the upstream solar wind $(n_0 = 10^{-10} n_{SW})$. Panels (i)–(l) depict the modeled bulk velocity for the traced particles in run #1, and the bottom row (panels (m)–(p)) shows the bulk velocity within the slice from run #3. This quantity is only plotted in regions where the number density of the test particles is larger than $5 \cdot 10^{-2} n_0$. The gray background in panels (i)–(p) indicates regions where the density remains below that threshold. From left to right the times $t_1, \ldots, t_4$ of the snapshots increase in increments of 6 s, and the traced proton slice move from upstream (positive X values) to downstream (negative X values). The initial snapshot at $t_1 = 0$ s is taken at the time when the traced slice of protons arrives at Mercury's dayside apex.

high-latitude BS (t_2) they become heated, that is, the distribution spreads out (panels 8(f) and 8(j)). At the same time the particles are decelerated in ($-X$) direction and are deflected northward. The bulk velocity is changed to approximately $(-u_X) = 700$ km s^{-1} and $u_Z = 100$ km s^{-1} (see also panels 7(b) and 7(j)). At t_4 the $(-u_X)$ component returns to the value in the upstream solar wind (800 km s^{-1}, see panel 8(h)). Simultaneously, the particles are further accelerated in Z direction, reaching $u_Z = 200$ km s^{-1}, and the distribution becomes more narrow (panel 8(l)). Overall, Figure 8 indicates that the proton clouds are initially generated by the impact of the upstream plasma onto Mercury's magnetosphere and the subsequent heating leads to their expansion.

In run #3 at $t_2 = 6$ s, the segments of the proton population north and south of Mercury are decelerated in the region between the BS and MP and perform an evasive motion toward the north or south (red and blue regions in

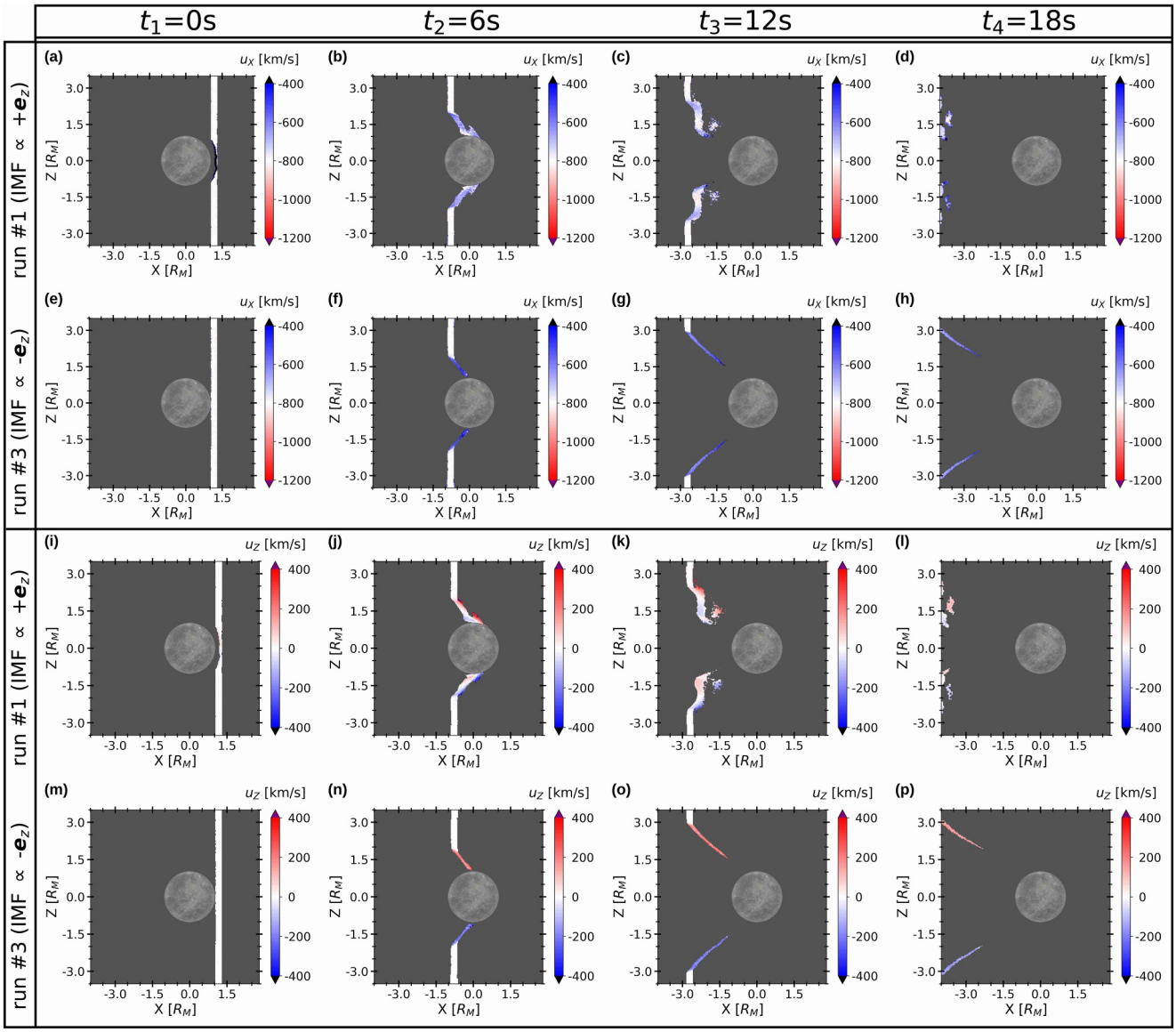

Figure 7. Components of the bulk velocity along the Mercury-Sun (u_X) and the south-north direction (u_Z), calculated for the "slice" of protons traced through the electromagnetic fields from runs #1 and #3. The first and second row display results for the u_X component of run #1 (panels (a)–(d)) and run #3 (panels (e)–(h)), respectively. The color bar used for u_X is centered around the value in the upstream solar wind (white, $u_X = -800$ km s^{-1}). Blue hue indicates that the magnitude of the velocity component toward downstream ($-u_X$) is reduced (i.e., the flow is decelerated) and red shaded areas mark acceleration of the bulk flow. The third and bottom row show the u_Z component for run #1 (panels (i)–(l)) and run #3 (panels (m)–(p)), respectively. The color bar used for u_Z is centered around the upstream value of $u_Z = 0$ km s^{-1} (white). Red hue indicates a northward deflection and regions colored in blue show a southward component of the bulk velocity. Similar to panels 6(i)–6(p), the gray background in all panels indicates regions where the number density of the traced proton population is smaller than 5% of the value in the upstream slice ($n_0 = 10^{-10} n_{SW}$). The times $t_1, \ldots, t_4$ of the snapshots are the same as in Figure 6. The traced proton slice propagates toward downstream (i.e., to decreasing X values) when going from the left to the right panels.

panel 7(n)). This behavior continues for the subsequent snapshots (t_3 and t_4). This means that even though there is no dayside boundary layer at low latitudes during DDM conditions, the BS and MP at high latitudes act as they would under nominal solar wind conditions.

In none of the snapshots the traced proton density exceeds $5 \cdot 10^{-2}\ n_0$ inside the magnetosphere for run #3, indicating that almost no particles enter this region for this setup. We continued the run up to $t = 22$ s. At this time all test particles from the marked slice have crossed the downstream face of the simulation box without any return flow toward Mercury occurring in the magnetotail. Sun, Slavin, Dewey, et al. (2020) studied MESSENGER

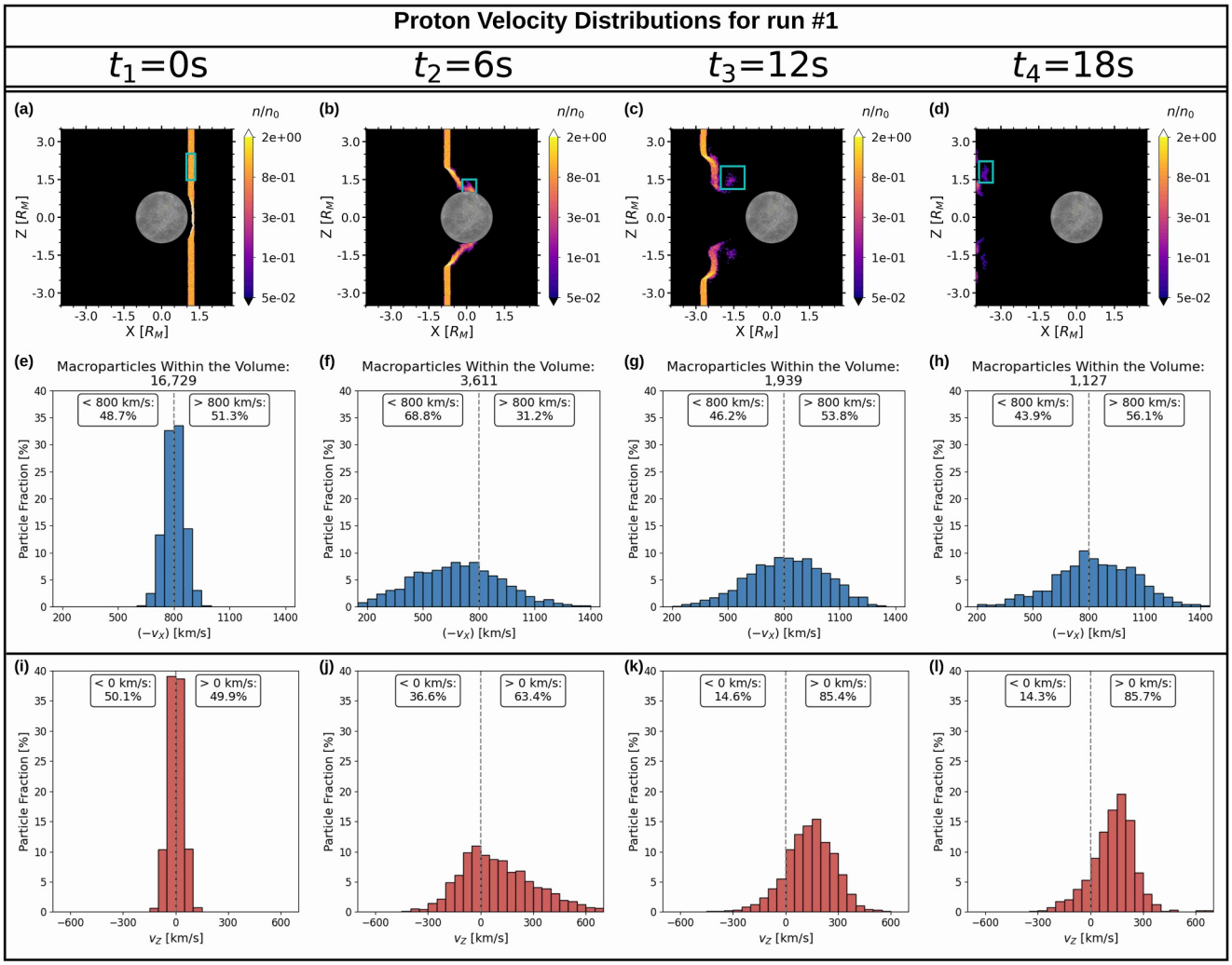

Figure 8. Evolution of the distributions for the velocity components of traced protons from run #1. The times $t_1, \ldots, t_4$ of the snapshots are the same as in Figures 6 and 7. The first row (panels (a)–(d)) shows, analogous to panels 6(a)–6(d), the number density of the traced particle population. The cyan rectangles in these panels mark the regions where the proton velocity distributions are sampled. We use a cuboid that extends from $-0.02\ R_M$ to $+0.02\ R_M$ in Y direction and along the marked rectangles in X and Z direction. We select all protons within these cuboids to calculate the velocity distributions. For $t_1 = 0$ s the sampling volume for the proton statistics covers the undisturbed solar wind upstream and north of Mercury. This snapshot establishes the baseline for the analysis of the subsequent distributions that are affected by the planet's magnetosphere. At times t_2, t_3, and t_4 the location and volume of the cuboids are adapted to capture the momentary position of the northern proton "cloud" near the magnetosphere (see text for details). The second row (panels (e)–(h)) displays the distribution of the $(-v_X)$ component for the protons inside the associated sampling volume and the third row (panels (i)–(l)) depicts the distribution for the v_Z component. In both rows the vertical gray dashed lines mark the value of the bulk velocity in the upstream solar wind ($-u_X = 800$ km s^{-1}, $u_Z = 0$ km s^{-1}). The boxes in the upper left and right corners of panels (e)–(l) indicate the fraction of protons that is slower or faster than the respective component of the upstream bulk velocity. Panels (e)–(h) also display the number of macroparticles within the sampling volume.

observations of a ICME impact onto Mercury, with the MP still residing above the surface, and reported the NMNL to be even closer to the planet at $|X| < 2.5\ R_M$ than under nominal solar wind conditions ($|X| < 3\ R_M$). Hence, if there was an NMNL present during the DDM event, it should be located inside of our model domain. Therefore, we do not expect a planetward flow of plasma in the tail to occur if we further increased the downstream extension of the simulation box. This means that no Dungey cycle can form under DDM conditions at Mercury: the solar wind merely travels along the outer boundaries of the magnetosphere from upstream to downstream. We attribute this to the absence of closed planetary field lines in the upstream hemisphere, inhibiting reconnection at both the dayside and the nightside.

4. Summary and Concluding Remarks

In this study, we have investigated how Mercury's magnetosphere behaves during DDM events. Such events are characterized by an enhanced upstream ram pressure, caused by an interplanetary Coronal Mass Ejection (ICME). This increased pressure pushes the dayside MP below the planet's surface. Four DDM events have been identified in observations from the MESSENGER magnetometer and FIPS instrument (Slavin et al., 2019; Winslow et al., 2020). The range of upstream pressures on these occasions was estimated to be 142 nPa–562 nPa, which is about an order of magnitude higher than under nominal solar wind conditions (Winslow et al., 2013). Our goal was to constrain how different IMF orientations, and consequently different dayside reconnection rates, influence the structure of the magnetosphere under these extreme solar wind conditions. In addition, our study provides context for the interpretation of magnetometer and plasma data from MESSENGER and the BepiColombo mission (Benkhoff et al., 2010, 2021), which is scheduled to arrive at Mercury in 2026.

We apply the AIKEF hybrid model (Müller et al., 2011), using a ram pressure of 385 nPa, as derived for the DDM event in 2013 (Winslow et al., 2020). We considered three idealized IMF orientations: northward (inhibiting dayside reconnection), southward (enhancing reconnection), and duskward (facilitating reconnection at the flanks of the magnetosphere). Furthermore, we carried out multiple model runs under steady-state upstream conditions to support the interpretation of MESSENGER magnetometer data from the 2013 DDM event (Slavin et al., 2019; Winslow et al., 2020). This event occurred over two consecutive MESSENGER orbits, each of them lasting 8 hours. Our work complements the study of Guo et al. (2023) who modeled Mercury's magnetosphere during DDM events for idealized north- and southward IMF setups. However, their approach considered ram pressures up to 107 nPa, which is below the range estimated for the observed DDM events. We point out that the (indirect) derivation of pressure values for these ICME events is afflicted with significant uncertainties. In addition to considering the reported values for the upstream pressure, our study takes into account highly inclined IMF orientations: for instance, during the 2013 DDM event the upstream field was tilted against the Sun-Mercury line by about 20°.

Our major results are as follows:

1. The solar wind is shocked upstream of Mercury for a northward or duskward IMF. For southward IMF, no BS forms at low latitudes upstream of Mercury. This locally results in a lunar-type interaction of the plasma: the solar wind impacts without prior deceleration onto the planet's surface. In this case, the model reveals no closed planetary field lines above the low-latitude dayside hemisphere.
2. For all studied IMF orientations, distinct boundary layers for the BS and MP are formed at high dayside latitudes and downstream of Mercury. The high-latitude BS affects the solar wind similar to nominal conditions: the velocity distributions of protons upstream and downstream of the shock reveal that the plasma is decelerated and heated when it crosses that boundary layer. For both northward and southward IMF, solar wind protons largely travel toward downstream along the outer flanks of the MP.
3. When the IMF points southward, the absence of closed planetary field lines upstream of Mercury inhibits the formation of a Dungey cycle. Within distances of about 4 R_M at the downstream side, corresponding to the extension of our model domain, AIKEF does not reveal any return flow of solar wind within the magnetotail. This distance covers the position of the Near Mercury Neutral Line under nominal solar wind conditions (3 R_M, see Poh et al., 2017) and for a low-pressure ICME impact that still allowed the dayside MP to reside above the surface (2.5 R_M, see Sun, Slavin, Dewey, et al., 2020).
4. The upstream pressure dropped while MESSENGER was inside of Mercury's magnetosphere during the first orbit of the 2013 DDM event. The draping pattern observed in the northern magnetotail lobe quantitatively agrees with a model output from a setup applying a ram pressure of 562 nPa. On the other hand, the draping signature seen in the southern lobe is best described by a model run using a lower pressure of 385 nPa. This drop in pressure would have occurred on a time scale of 1 hour, corresponding to the duration of MESSENGER's passage through the magnetotail. The notion of a reduction in pressure during the 2013 DDM event is qualitatively consistent with the results of Slavin et al. (2019), who reported a lower value of 182 nPa during MESSENGER's second orbit compared to the first one (385 nPa, see Winslow et al., 2020).
5. The IMF vector changed from possessing a duskward to having a dawnward component while MESSENGER was inside Mercury's magnetosphere during the first orbit of the 2013 DDM event. The perturbations to the dawn-dusk component of the magnetic field observed during MESSENGER's crossing of the BS likely stem from the interaction with an IMF vector that has a duskward component. Conversely, the observed position of

the neutral sheet in the magnetotail could only be explained when including an IMF with a dawnward component.

6. The southward displacement of the neutral sheet observed during the 2013 DDM event (Winslow et al., 2020) may have been caused by magnetotail twisting due to a dawnward component of the IMF. Under DDM conditions the tail is rotated clockwise (counterclockwise) around a straight line parallel to the Sun-Mercury line and going through the planet's dipole moment when the IMF possesses a dawnward (duskward) component. This is the same relation between IMF orientation and tail twisting as reported by Romanelli et al. (2022) for MESSENGER observations under nominal solar wind conditions at Mercury.

The inductive response of Mercury's core to time-varying upstream conditions, as observed during the 2013 DDM event, can push the MP farther sunward (e.g., Glassmeier et al., 2007; Heyner et al., 2016; Jia et al., 2019). The role of time-dependent upstream conditions during a DDM event has been modeled by Guo et al. (2023). These authors used a purely southward IMF and varied the field magnitude. In addition, they increased the upstream ram pressure from 8 nPa (corresponding to nominal conditions) to a maximum value of 107 nPa. Hence, future work is needed to cover the high pressure regime that was estimated for DDM events at Mercury and search the sampled magnetometer time series for signs of induction. Furthermore, it should be investigated how changes of the IMF orientation, as observed during the 2013 DDM event, map into the inductive response.

Appendix A: Influence of the Upstream Ram Pressure on Mercury's Magnetosphere During DDM Events

To determine the influence of the upstream pressure on Mercury's magnetosphere during DDM events, we compare two runs using solar wind conditions from the events with the highest estimated ram pressure (run #3, corresponding to the 2013 DDM event, Winslow et al., 2020) and the lowest value (run #6, corresponding to the 2011 DDM event, Slavin et al., 2019). In both runs, the IMF is oriented in $(-Z)$ direction. Detailed information on the used setups can be found in Table 1 and Section 2. Figure A1 shows the AIKEF output for runs #3 (first row) and #6 (second row).

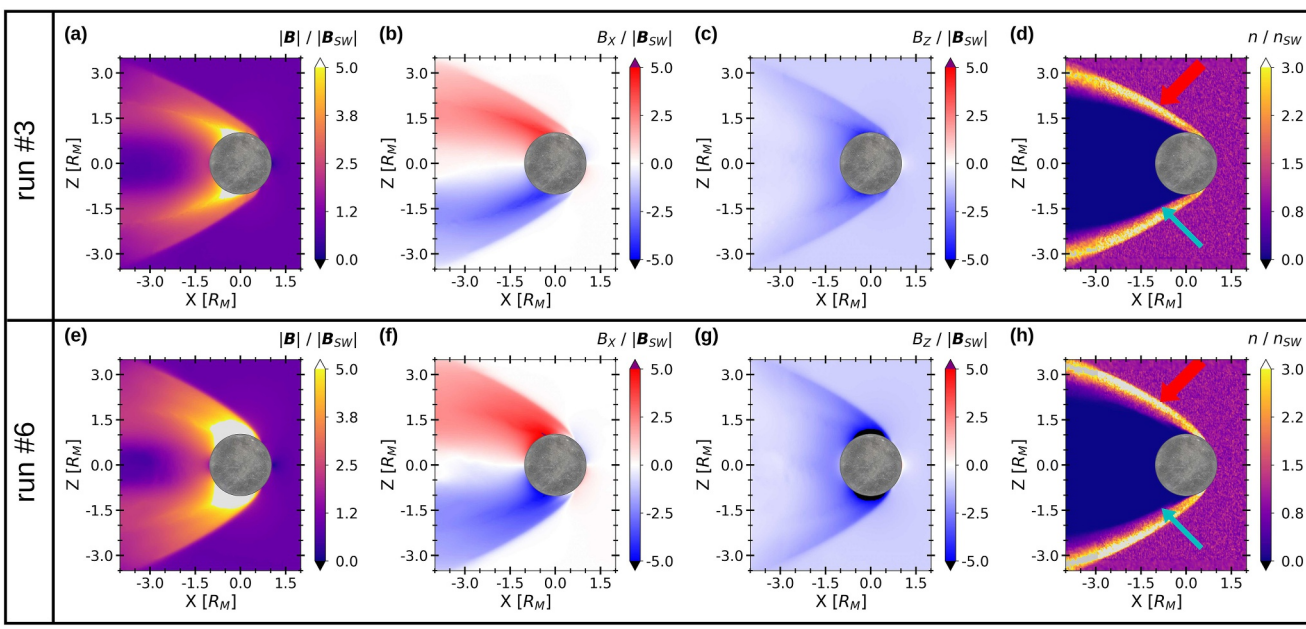

Figure A1. Comparison of the AIKEF mod1el results from runs #3 and #6. The first row depicts the output of run #3 and the bottom row displays results from run #6. The results for run #3 have already been shown in Figures 1 and 2 and are presented here again to facilitate comparison. All panels display plasma quantities in the $X - Z$-plane. From left to right, the columns depict the magnetic field magnitude (panels (a), (e)), the B_X component (panels (b), (f)), the B_Z component (panels (c), (g)), and the proton number density (panels (d), (h)). For the ease of comparison, all quantities are normalized to the upstream solar wind values: $|\boldsymbol{B}_{SW}| = 115$ nT; $n_{SW} = 360\,\mathrm{cm}^{-3}$ for run #3 and $|\boldsymbol{B}_{SW}| = 68$ nT; $n_{SW} = 105\,\mathrm{cm}^{-3}$ for run #6. The arrows in panels (d) and (h) mark the modeled magnetopause (cyan) and bow shock (bold red).

The qualitative structure of the magnetosphere is similar for both setups. The jumps in the proton number density on Mercury's nightside show a parabolic BS and MP downstream of the planet. Two lobes can be seen in the magnetic field on the planet's nightside (panels A1(a), (b) and (e), (f)). For both runs $|B_X|$ in the lobes reaches values of up to four times the respective IMF magnitude. On the dayside no density pileup is formed close to the subsolar point and no closed planetary field lines are present above the dayside in these runs, indicating that Mercury's low-latitude surface is directly exposed to the unshocked solar wind. Slavin et al. (2019) identified BS crossings in MESSENGER magnetometer data and found the subsolar BS to be located approximately 0.5 R_M above Mercury's dayside surface for the 2011 DDM event. In contrast to this, results from run #6 do not reveal a BS upstream of Mercury. However, the presence of such a structure during DDM events strongly depends on the IMF orientation (see Section 3.1). The observed upstream field during the 2011 event possesses almost equal components in the directions of all three coordinate axes, while run #6 applies an IMF entirely in $(-Z)$ direction. Therefore, the absence of a low-latitude BS in our model results is not in contradiction to the observations of Slavin et al. (2019).

Appendix B: Contribution of the Offset Dipole in the MSM System

Figure B1 displays the difference between the magnetic fields from runs #4 and #3 in Mercury-Solar-Magnetospheric (MSM) coordinates (X_{MSM}, Y_{MSM}, Z_{MSM}). The axes of this system are parallel to those of the MSO coordinates, but its origin coincides with the planetary dipole moment (and *not* Mercury's center).

Comparison to Panels 3(b) and 3(c) illustrates that the differences in MSM coordinates are slightly weaker than in MSO, but still of the same order of magnitude. Under DDM conditions, both deflection by the internal dipole and particle absorption at Mercury's surface make contributions to the plasma flow pattern and associated currents near the planet. Hence, it is not unexpected that the differences are comparable between both coordinate systems.

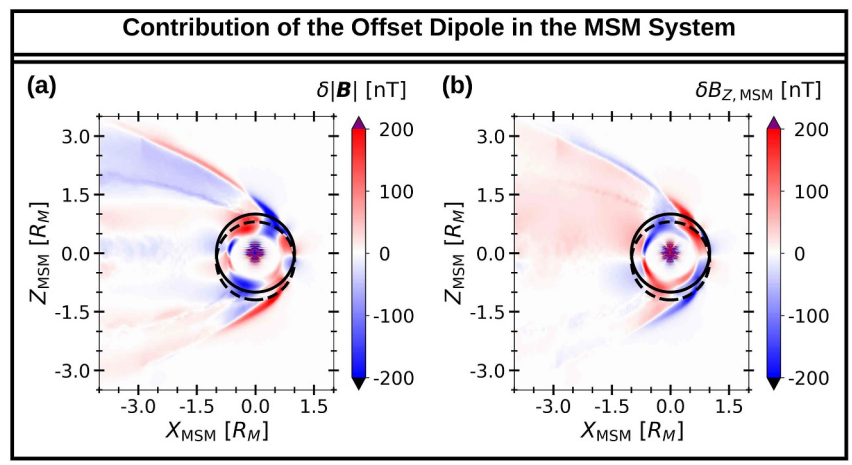

Figure B1. Difference between model results from runs #4 and #3, but displayed in MSM coordinates. The quantities shown in these plots have been computed analogous to panels 3(b) and 3(c). The solid black circle denotes the location of Mercury in run #3 (centered dipole), whereas the dashed black circle shows the planet's position in run #4 (offset dipole).

Conflict of Interest

The authors declare no conflicts of interest relevant to this study.

Data Availability Statement

The data set used to generate the figures in this work can be obtained from Glebe et al. (2025). The MESSENGER magnetometer data is publicly available on the NASA Planetary Data System (Korth, 2021).

Acknowledgments
The authors acknowledge financial support through NASA's *Solar System Workings* program, Grant 80NSSC24K0099. The computing resources used to carry out the AIKEF runs were provided by the NASA High-End Computing Program through the NASA Advanced Supercomputing Division at Ames Research Center. Furthermore, the authors would like to thank Neil E. Baker (Georgia Institute of Technology) whose particle tracing tool was used to support generation of Figure 8. This body of work was not written nor contributed to in any part by an artificial intelligence engine.

References

Aizawa, S., Griton, L. S., Fatemi, S., Exner, W., Deca, J., Pantellini, F., et al. (2021). Cross-comparison of global simulation models applied to Mercury's dayside magnetosphere. *Planetary and Space Science*, *198*, 105176. https://doi.org/10.1016/j.pss.2021.105176

Anderson, B. J., Acuña, M. H., Lohr, D. A., Scheifele, J., Raval, A., Korth, H., & Slavin, J. A. (2007). The magnetometer instrument on MESSENGER. *Space Science Reviews*, *131*(1–4), 417–450. https://doi.org/10.1007/s11214-007-9246-7

Anderson, B. J., Johnson, C. L., Korth, H., Purucker, M. E., Winslow, R. M., Slavin, J. A., et al. (2011). The global magnetic field of Mercury from MESSENGER orbital observations. *Science*, *333*(6051), 1859–1862. https://doi.org/10.1126/science.1211001

Anderson, B. J., Johnson, C. L., Korth, H., Winslow, R. M., Borovsky, J. E., Purucker, M. E., et al. (2012). Low-degree structure in Mercury's planetary magnetic field. *Journal of Geophysical Research (Planets)*, *117*(E12), E00L12. https://doi.org/10.1029/2012JE004159

Andrews, G. B., Zurbuchen, T. H., Mauk, B. H., Malcom, H., Fisk, L. A., Gloeckler, G., et al. (2007). The energetic particle and plasma spectrometer instrument on the MESSENGER spacecraft. *Space Science Reviews*, *131*(1–4), 523–556. https://doi.org/10.1007/s11214-007-9272-5

Benkhoff, J., Murakami, G., Baumjohann, W., Besse, S., Bunce, E., Casale, M., et al. (2021). BepiColombo - Mission overview and science goals. *Space Science Reviews*, *217*(8), 90. https://doi.org/10.1007/s11214-021-00861-4

Benkhoff, J., van Casteren, J., Hayakawa, H., Fujimoto, M., Laakso, H., Novara, M., et al. (2010). BepiColombo—Comprehensive exploration of Mercury: Mission overview and science goals. *Planetary and Space Science*, *58*(1–2), 2–20. https://doi.org/10.1016/j.pss.2009.09.020

Bowers, C. F., Jackman, C. M., Jia, X., Slavin, J. A., Saur, J., Holmberg, M. K. G., et al. (2025). MESSENGER observations of a possible alfvén wing at Mercury driven by a low alfvénic Mach number Interplanetary coronal Mass ejection. *Journal of Geophysical Research (Space Physics)*, *130*(3), 2024JA033619. https://doi.org/10.1029/2024JA033619

Burlaga, L. F. (1988). Magnetic clouds and force-free fields with constant alpha. *Journal of Geophysical Research*, *93*(A7), 7217–7224. https://doi.org/10.1029/JA093iA07p07217

Dong, C., Wang, L., Hakim, A., Bhattacharjee, A., Slavin, J. A., DiBraccio, G. A., & Germaschewski, K. (2019). Global ten-moment multifluid simulations of the solar wind interaction with Mercury: From the planetary conducting core to the dynamic magnetosphere. *Geophysical Research Letters*, *46*(21), 11584–11596. https://doi.org/10.1029/2019GL083180

Exner, W., Griton, L. S., & Heyner, D. (2024). Determining the influence of the IMF and planetary magnetic field models on mercury's magnetosphere along spacecraft trajectories of MESSENGER, BepiColombo and MPO. *Journal of Geophysical Research (Space Physics)*, *129*(3), e2023JA032248. https://doi.org/10.1029/2023JA032248

Exner, W., Heyner, D., Liuzzo, L., Motschmann, U., Shiota, D., Kusano, K., & Shibayama, T. (2018). Coronal mass ejection hits mercury: A.I.K. E.F. hybrid-code results compared to MESSENGER data. *Planetary and Space Science*, *153*, 89–99. https://doi.org/10.1016/j.pss.2017.12.016

Exner, W., Simon, S., Heyner, D., & Motschmann, U. (2020). Influence of mercury's exosphere on the structure of the magnetosphere. *Journal of Geophysical Research (Space Physics)*, *125*(7), e27691. https://doi.org/10.1029/2019JA027691

Fairfield, D. H., & Behannon, K. W. (1976). Bow Shock and magnetosheath waves at Mercury. *Journal of Geophysical Research*, *81*(22), 3897–3906. https://doi.org/10.1029/JA081i022p03897

Fatemi, S., HolmströM, M., Futaana, Y., Barabash, S., & Lue, C. (2013). The lunar wake current systems. *Geophysical Research Letters*, *40*(1), 17–21. https://doi.org/10.1029/2012GL054635

Fatemi, S., Poppe, A. R., & Barabash, S. (2020). Hybrid simulations of solar wind proton precipitation to the surface of Mercury. *Journal of Geophysical Research (Space Physics)*, *125*(4), e27706. https://doi.org/10.1029/2019JA027706

Finlay, C. C., Maus, S., Beggan, C. D., Bondar, T. N., Chambodut, A., Chernova, T. A., et al. (2010). International Geomagnetic Reference Field: The eleventh generation. *Geophysical Journal International*, *183*(3), 1216–1230. https://doi.org/10.1111/j.1365-246X.2010.04804.x

Gamborino, D., Vorburger, A., & Wurz, P. (2019). Mercury's subsolar sodium exosphere: An ab initio calculation to interpret MASCS/UVVS observations from MESSENGER. *Annales Geophysicae*, *37*(4), 455–470. https://doi.org/10.5194/angeo-37-455-2019

Gershman, D. J., Slavin, J. A., Raines, J. M., Zurbuchen, T. H., Anderson, B. J., Korth, H., et al. (2014). Ion kinetic properties in Mercury's pre-midnight plasma sheet. *Geophysical Research Letters*, *41*(16), 5740–5747. https://doi.org/10.1002/2014GL060468

Glassmeier, K.-H., Grosser, J., Auster, U., Constantinescu, D., Narita, Y., & Stellmach, S. (2007). Electromagnetic induction effects and dynamo action in the hermean System. *Space Science Reviews*, *132*(2–4), 511–527. https://doi.org/10.1007/s11214-007-9244-9

Glebe, G., Haynes, C. M., & Simon, S. (2025). Data for "Compression of Mercury's Dayside Magnetopause to the Surface: A Three-Dimensional Model of Magnetospheric Structure and Dynamics" by Glebe et al [Dataset]. *Zenodo*. https://doi.org/10.5281/zenodo.16539383

Good, S. W., & Forsyth, R. J. (2016). Interplanetary coronal mass ejections observed by MESSENGER and Venus Express. *Solar Physics*, *291*(1), 239–263. https://doi.org/10.1007/s11207-015-0828-3

Grosser, J., Glassmeier, K. H., & Stadelmann, A. (2004). Induced magnetic field effects at planet Mercury. *Planetary and Space Science*, *52*(14), 1251–1260. https://doi.org/10.1016/j.pss.2004.08.005

Guo, J., Lu, S., Lu, Q., Slavin, J. A., Sun, W., Ren, J., et al. (2023). Three-Dimensional global hybrid simulations of mercury's disappearing dayside magnetosphere. *Journal of Geophysical Research (Planets)*, *128*(12), e2023JE008032. https://doi.org/10.1029/2023JE008032

Hauck, S. A., Margot, J.-L., Solomon, S. C., Phillips, R. J., Johnson, C. L., Lemoine, F. G., et al. (2013). The curious case of Mercury's internal structure. *Journal of Geophysical Research (Planets)*, *118*(6), 1204–1220. https://doi.org/10.1002/jgre.20091

Haynes, C. M., Simon, S., & Liuzzo, L. (2025). Emission of energetic neutral atoms from Ganymede's Magnetosphere-Atmosphere interaction. *Journal of Geophysical Research (Space Physics)*, *130*(10), e2025JA034469. https://doi.org/10.1029/2025JA034469

Heyner, D., Nabert, C., Liebert, E., & Glassmeier, K.-H. (2016). Concerning reconnection-induction balance at the magnetopause of Mercury. *Journal of Geophysical Research (Space Physics)*, *121*(4), 2935–2961. https://doi.org/10.1002/2015JA021484

Heyner, D., Schmitt, D., Wicht, J., Glassmeier, K.-H., Korth, H., & Motschmann, U. (2010). The initial temporal evolution of a feedback dynamo for Mercury. *Geophysical & Astrophysical Fluid Dynamics*, *104*(4), 419–429. https://doi.org/10.1080/03091921003776839

Heyner, D., Wicht, J., Gómez-Pérez, N., Schmitt, D., Auster, H.-U., & Glassmeier, K.-H. (2011). Evidence from numerical experiments for a feedback dynamo generating mercury's magnetic field. *Science*, *334*(6063), 1690–1693. https://doi.org/10.1126/science.1207290

Hundhausen, A. J. (1970). Composition and dynamics of the solar wind plasma. *Reviews of Geophysics*, *8*(4), 729–811. https://doi.org/10.1029/RG008i004p00729

James, M. K., Imber, S. M., Bunce, E. J., Yeoman, T. K., Lockwood, M., Owens, M. J., & Slavin, J. A. (2017). Interplanetary magnetic field properties and variability near Mercury's orbit. *Journal of Geophysical Research (Space Physics)*, *122*(8), 7907–7924. https://doi.org/10.1002/2017JA024435

Jarvinen, R., Alho, M., Kallio, E., & Pulkkinen, T. I. (2019). Ultra-low-frequency waves in the ion foreshock of Mercury: A global hybrid modelling study. *Monthly Notices of the Royal Astronomical Society*, *491*(3), 4147–4161. https://doi.org/10.1093/mnras/stz3257

Jia, X., Slavin, J. A., Gombosi, T. I., Daldorff, L. K. S., Toth, G., & Holst, B. (2015). Global MHD simulations of Mercury's magnetosphere with coupled planetary interior: Induction effect of the planetary conducting core on the global interaction. *Journal of Geophysical Research (Space Physics)*, *120*(6), 4763–4775. https://doi.org/10.1002/2015JA021143

Jia, X., Slavin, J. A., Poh, G., DiBraccio, G. A., Toth, G., Chen, Y., et al. (2019). MESSENGER observations and global simulations of highly compressed magnetosphere events at Mercury. *Journal of Geophysical Research (Space Physics)*, *124*(1), 229–247. https://doi.org/10.1029/2018JA026166

Kabin, K., Gombosi, T. I., DeZeeuw, D. L., & Powell, K. G. (2000). Interaction of Mercury with the solar wind. *Icarus*, *143*(2), 397–406. https://doi.org/10.1006/icar.1999.6252

Korth, H. (2021). MESSENGER MAG calibrated MSO coordinates science data collection [Dataset]. *NASA Planetary Data System*. https://doi.org/10.17189/1522385

Korth, H., Anderson, B. J., Johnson, C. L., Slavin, J. A., Raines, J. M., & Zurbuchen, T. H. (2018). Structure and configuration of mercury's magnetosphere. In S. C. Solomon, L. R. Nittler, & B. J. Anderson (Eds.), *Mercury. the view after messenger* (pp. 430–460). Cambridge University Press. https://doi.org/10.1017/9781316650684.017

Le, G., Chi, P. J., Blanco-Cano, X., Boardsen, S., Slavin, J. A., Anderson, B. J., & Korth, H. (2013). Upstream ultra-low frequency waves in Mercury's foreshock region: MESSENGER magnetic field observations. *Journal of Geophysical Research (Space Physics)*, *118*(6), 2809–2823. https://doi.org/10.1002/jgra.50342

Leyser, R. P., Imber, S. M., Milan, S. E., & Slavin, J. A. (2017). The influence of IMF clock angle on dayside flux transfer events at Mercury. *Geophysical Research Letters*, *44*(21), 10829–10837. https://doi.org/10.1002/2017GL074858

Li, C., Jia, X., Chen, Y., Toth, G., Zhou, H., Slavin, J. A., et al. (2024). Kinetic signatures, dawn-dusk asymmetries, and flux transfer events associated with mercury's dayside magnetopause reconnection from 3D MHD-AEPIC simulations. *Journal of Geophysical Research (Space Physics)*, *129*(6), e2024JA032669. https://doi.org/10.1029/2024JA032669

Massetti, S., Orsini, S., Milillo, A., Mura, A., De Angelis, E., Lammer, H., & Wurz, P. (2003). Mapping of the cusp plasma precipitation on the surface of Mercury. *Icarus*, *166*(2), 229–237. https://doi.org/10.1016/j.icarus.2003.08.005

McClintock, W. E., Cassidy, T. A., Merkel, A. W., Killen, R. M., Burger, M. H., & Vervack, R. J. (2018). Observations of mercury's exosphere: Composition and structure. In S. C. Solomon, L. R. Nittler, & B. J. Anderson (Eds.), *Mercury. The view after MESSENGER* (pp. 371–406). Cambridge University Press. https://doi.org/10.1017/9781316650684.015

Müller, J., Simon, S., Motschmann, U., Schüle, J., Glassmeier, K.-H., & Pringle, G. J. (2011). A.I.K.E.F.: Adaptive hybrid model for space plasma simulations. *Computer Physics Communications*, *182*(4), 946–966. https://doi.org/10.1016/j.cpc.2010.12.033

Müller, J., Simon, S., Wang, Y.-C., Motschmann, U., Heyner, D., Schüle, J., et al. (2012). Origin of Mercury's double magnetopause: 3D hybrid simulation study with A. *I.K.E.F. Icarus*, *218*(1), 666–687. https://doi.org/10.1016/j.icarus.2011.12.028

Ness, N. F., Behannon, K. W., Lepping, R. P., Whang, Y. C., & Schatten, K. H. (1974). Magnetic field observations near Mercury: Preliminary results from mariner 10. *Science*, *185*(4146), 151–160. https://doi.org/10.1126/science.185.4146.151

Poh, G., Slavin, J. A., Jia, X., Raines, J. M., Imber, S. M., Sun, W.-J., et al. (2017). Mercury's cross-tail current sheet: Structure, X-line location and stress balance. *Geophysical Research Letters*, *44*(2), 678–686. https://doi.org/10.1002/2016GL071612

Pump, K., Heyner, D., Blanco Cano, X., Schmid, D., Sun, W., Narita, Y., & Plaschke, F. (2025). Bow shock crossing observations by MESSENGER from a magnetic point of view. *Journal of Geophysical Research (Space Physics)*, *130*(10), e2025JA034009. https://doi.org/10.1029/2025JA034009

Raines, J. M., Slavin, J. A., Zurbuchen, T. H., Gloeckler, G., Anderson, B. J., Baker, D. N., et al. (2011). MESSENGER observations of the plasma environment near Mercury. *Planetary and Space Science*, *59*(15), 2004–2015. https://doi.org/10.1016/j.pss.2011.02.004

Rasca, A. P., Fatemi, S., & Farrell, W. M. (2022). Modeling the lunar wake response to a CME using a hybrid PIC model. *The Planetary Science Journal*, *3*(1), 4. https://doi.org/10.3847/PSJ/ac3fba

Rasca, A. P., Fatemi, S., Farrell, W. M., Poppe, A. R., & Zheng, Y. (2021). A double disturbed lunar plasma wake. *Journal of Geophysical Research (Space Physics)*, *126*(2), e28789. https://doi.org/10.1029/2020JA028789

Romanelli, N., & DiBraccio, G. A. (2021). Occurrence rate of ultra-low frequency waves in the foreshock of Mercury increases with heliocentric distance. *Nature Communications*, *12*(1), 6748. https://doi.org/10.1038/s41467-021-26344-2

Romanelli, N., DiBraccio, G. A., Slavin, J., Bowers, C., & Weber, T. (2022). The search for magnetotail twisting at Mercury: Comparing MESSENGER observations with the terrestrial case. *Geophysical Research Letters*, *49*(24), e2022GL101643. https://doi.org/10.1029/2022GL101643

Sarantos, M., & Slavin, J. A. (2009). On the possible formation of Alfvén wings at Mercury during encounters with coronal mass ejections. *Geophysical Research Letters*, *36*(4), L04107. https://doi.org/10.1029/2008GL036747

Shue, J. H., Chao, J. K., Fu, H. C., Russell, C. T., Song, P., Khurana, K. K., & Singer, H. J. (1997). A new functional form to study the solar wind control of the magnetopause size and shape. *Journal of Geophysical Research*, *102*(A5), 9497–9512. https://doi.org/10.1029/97JA00196

Siegfried, R. W., II, & Solomon, S. C. (1974). Mercury: Internal structure and thermal evolution. *Icarus*, *23*(2), 192–205. https://doi.org/10.1016/0019-1035(74)90005-0

Simon, S., Bagdonat, T., Motschmann, U., & Glassmeier, K. H. (2006). Plasma environment of magnetized asteroids: A 3-D hybrid simulation study. *Annales Geophysicae*, *24*(1), 407–414. https://doi.org/10.5194/angeo-24-407-2006

Slavin, J. A., Acuña, M. H., Anderson, B. J., Baker, D. N., Benna, M., Boardsen, S. A., et al. (2009). MESSENGER observations of magnetic reconnection in mercury's magnetosphere. *Science*, *324*(5927), 606–610. https://doi.org/10.1126/science.1172011

Slavin, J. A., Anderson, B. J., Baker, D. N., Benna, M., Boardsen, S. A., Gloeckler, G., et al. (2010). MESSENGER observations of extreme loading and unloading of mercury's magnetic tail. *Science*, *329*(5992), 665–668. https://doi.org/10.1126/science.1188067

Slavin, J. A., DiBraccio, G. A., Gershman, D. J., Imber, S. M., Poh, G. K., Raines, J. M., et al. (2014). MESSENGER observations of Mercury's dayside magnetosphere under extreme solar wind conditions. *Journal of Geophysical Research (Space Physics)*, *119*(10), 8087–8116. https://doi.org/10.1002/2014JA020319

Slavin, J. A., & Holzer, R. E. (1981). Solar wind flow about the terrestrial planets, 1. Modeling bow shock position and shape. *Journal of Geophysical Research*, *86*(A13), 11401–11418. https://doi.org/10.1029/JA086iA13p11401

Slavin, J. A., Imber, S. M., & Raines, J. M. (2021). A dungey cycle in the life of mercurys magnetosphere. In R. Maggiolo, N. André, H. Hasegawa, & D. T. Welling (Eds.), *Magnetospheres in the solar System* (Vol. 2, pp. 537–556). American Geophysical Union (AGU). https://doi.org/10.1002/9781119815624.ch34

Slavin, J. A., Middleton, H. R., Raines, J. M., Jia, X., Zhong, J., Sun, W. J., et al. (2019). MESSENGER observations of disappearing dayside magnetosphere events at Mercury. *Journal of Geophysical Research (Space Physics)*, *124*(8), 6613–6635. https://doi.org/10.1029/2019JA026892

Smith, D. E., Zuber, M. T., Phillips, R. J., Solomon, S. C., Hauck, S. A., Lemoine, F. G., et al. (2012). Gravity field and internal structure of Mercury from MESSENGER. *Science*, *336*(6078), 214–217. https://doi.org/10.1126/science.1218809

Song, P., Gombosi, T. I., DeZeeuw, D. L., Powell, K. G., & Groth, C. P. T. (2000). A model of solar wind-magnetosphere-ionosphere coupling for due northward IMF. *Planetary and Space Science*, *48*(1), 29–39. https://doi.org/10.1016/S0032-0633(99)00065-3

Spreiter, J. R., Summers, A. L., & Alksne, A. Y. (1966). Hydromagnetic flow around the magnetosphere. *Planetary and Space Science*, *14*(3), 223–253. https://doi.org/10.1016/0032-0633(66)90124-3

Stahl, A., Addison, P., Simon, S., & Liuzzo, L. (2023). A model of ganymede's magnetic and plasma environment during the Juno PJ34 flyby. *Journal of Geophysical Research (Space Physics)*, *128*(12), e2023JA032113. https://doi.org/10.1029/2023JA032113

Suess, S. T., & Goldstein, B. E. (1979). Compression of the Hermaean magnetosphere by the solar wind. *Journal of Geophysical Research*, *84*(A7), 3306–3312. https://doi.org/10.1029/JA084iA07p03306

Sun, W. J., Dewey, R. M., Aizawa, S., Huang, J., Slavin, J. A., Fu, S., et al. (2022). Review of Mercury's dynamic magnetosphere: Post-MESSENGER era and comparative magnetospheres. *Science China Earth Sciences*, *65*(1), 25–74. https://doi.org/10.1007/s11430-021-9828-0

Sun, W. J., Slavin, J. A., Dewey, R. M., Chen, Y., DiBraccio, G. A., Raines, J. M., et al. (2020). MESSENGER observations of mercury's nightside magnetosphere under extreme solar wind conditions: Reconnection-generated structures and steady convection. *Journal of Geophysical Research (Space Physics)*, *125*(3), e27490. https://doi.org/10.1029/2019JA027490

Sun, W. J., Slavin, J. A., Smith, A. W., Dewey, R. M., Poh, G. K., Jia, X., et al. (2020). Flux transfer event showers at Mercury: Dependence on Plasma β and magnetic shear and their contribution to the dungey cycle. *Geophysical Research Letters*, *47*(21), e89784. https://doi.org/10.1029/2020GL089784

Teubenbacher, D., Exner, W., Feyerabend, M., Narita, Y., Schmid, D., Laky, G., et al. (2024). Solar wind entry into Mercury's magnetosphere: Simulation results for the second swingby of BepiColombo. *Astronomy and Astrophysics*, *681*, A98. https://doi.org/10.1051/0004-6361/202347789

Teubenbacher, D., Exner, W., Narita, Y., Varsani, A., Schmid, D., Jeszenszky, H., et al. (2025). Hybrid modeling of Mercury's magnetosphere: Assessing accuracy in ion counting statistics. *Astronomy and Astrophysics*, *698*, A12. https://doi.org/10.1051/0004-6361/202453452

Teubenbacher, D., Narita, Y., Varsani, A., Schmid, D., Laky, G., & Exner, W. (2025). Ion-kinetic modeling of Mercury's magnetosphere: A reference for BepiColombo's sixth flyby. *Earth Planets and Space*, *77*(1), 109. https://doi.org/10.1186/s40623-025-02231-8

Thébault, E., Langlais, B., Oliveira, J. S., Amit, H., & Leclercq, L. (2018). A time-averaged regional model of the Hermean magnetic field. *Physics of the Earth and Planetary Interiors*, *276*, 93–105. https://doi.org/10.1016/j.pepi.2017.07.001

Töpfer, S., Narita, Y., Exner, W., Heyner, D., Kolhey, P., Glassmeier, K. H., & Motschmann, U. (2021). The Mie representation for Mercury's magnetospheric currents. *Earth Planets and Space*, *73*(1), 204. https://doi.org/10.1186/s40623-021-01536-8

Töpfer, S., Narita, Y., Glassmeier, K. H., Heyner, D., Kolhey, P., Motschmann, U., & Langlais, B. (2021). The Mie representation for Mercury's magnetic field. *Earth Planets and Space*, *73*(1), 65. https://doi.org/10.1186/s40623-021-01386-4

Töpfer, S., Narita, Y., Heyner, D., & Motschmann, U. (2020). The Capon method for Mercury's magnetic field analysis. *Frontiers in Physics*, *8*, 249. https://doi.org/10.3389/fphy.2020.00249

Töpfer, S., Oertel, I., Schiron, V., Narita, Y., Glassmeier, K.-H., Heyner, D., & Motschmann, U. (2022). Reconstruction of Mercury's internal magnetic field beyond the octupole. *Annales Geophysicae*, *40*(1), 91–105. https://doi.org/10.5194/angeo-40-91-2022

Varela, J., Pantellini, F., & Moncuquet, M. (2016). Parametric study of the solar wind interaction with the Hermean magnetosphere for a weak interplanetary magnetic field. *Planetary and Space Science*, *120*, 78–86. https://doi.org/10.1016/j.pss.2015.11.011

Wardinski, I., Langlais, B., & Thébault, E. (2019). Correlated time-varying magnetic fields and the core size of Mercury. *Journal of Geophysical Research (Planets)*, *124*(8), 2178–2197. https://doi.org/10.1029/2018JE005835

Werner, A. L. E., Aizawa, S., Leblanc, F., Chaufray, J. Y., Modolo, R., Raines, J. M., et al. (2022). Ion density and phase space density distribution of planetary ions Na^+, O^+ and He^+ in Mercury's magnetosphere. *Icarus*, *372*, 114734. https://doi.org/10.1016/j.icarus.2021.114734

Winslow, R. M., Anderson, B. J., Johnson, C. L., Slavin, J. A., Korth, H., Purucker, M. E., et al. (2013). Mercury's magnetopause and bow shock from MESSENGER Magnetometer observations. *Journal of Geophysical Research (Space Physics)*, *118*(5), 2213–2227. https://doi.org/10.1002/jgra.50237

Winslow, R. M., Johnson, C. L., Anderson, B. J., Gershman, D. J., Raines, J. M., Lillis, R. J., et al. (2014). Mercury's surface magnetic field determined from proton-reflection magnetometry. *Geophysical Research Letters*, *41*(13), 4463–4470. https://doi.org/10.1002/2014GL060258

Winslow, R. M., Lugaz, N., Philpott, L., Farrugia, C. J., Johnson, C. L., Anderson, B. J., et al. (2020). Observations of extreme ICME ram pressure compressing mercury's dayside magnetosphere to the surface. *The Astrophysical Journal*, *889*(2), 184. https://doi.org/10.3847/1538-4357/ab6170

Winslow, R. M., Lugaz, N., Philpott, L. C., Schwadron, N. A., Farrugia, C. J., Anderson, B. J., & Smith, C. W. (2015). Interplanetary coronal mass ejections from MESSENGER orbital observations at Mercury. *Journal of Geophysical Research (Space Physics)*, *120*(8), 6101–6118. https://doi.org/10.1002/2015JA021200

Winslow, R. M., Philpott, L., Paty, C. S., Lugaz, N., Schwadron, N. A., Johnson, C. L., & Korth, H. (2017). Statistical study of ICME effects on Mercury's magnetospheric boundaries and northern cusp region from MESSENGER. *Journal of Geophysical Research (Space Physics)*, *122*(5), 4960–4975. https://doi.org/10.1002/2016JA023548

Zhong, J., Wan, W. X., Slavin, J. A., Wei, Y., Lin, R. L., Chai, L. H., et al. (2015). Mercury's three-dimensional asymmetric magnetopause. *Journal of Geophysical Research (Space Physics)*, *120*(9), 7658–7671. https://doi.org/10.1002/2015JA021425

Zhong, J., & Wang, Y. (2024). Global magnetic field properties in the solar wind interaction of Mercury from MESSENGER measurements. *Astronomy and Astrophysics*, *692*, A136. https://doi.org/10.1051/0004-6361/202451926

Zomerdijk-Russell, S., Masters, A., & Heyner, D. (2021). Variability of the interplanetary magnetic field as a driver of electromagnetic induction in mercury's interior. *Journal of Geophysical Research (Space Physics)*, *126*(10), e29664. https://doi.org/10.1029/2021JA029664

Zomerdijk-Russell, S., Masters, A., Sun, W. J., Fear, R. C., & Slavin, J. A. (2023). Does reconnection only occur at points of maximum shear on mercury's dayside magnetopause? *Journal of Geophysical Research (Space Physics)*, *128*(11), e2023JA031810. https://doi.org/10.1029/2023JA031810